3-D pore-scale resolved model for coupled species/charge/fluid transport in a vanadium redox flow battery

Gang Qiu [a], Abhijit S. Joshi [a], C.R. Dennison [b], K.W. Knehr [b], E.C. Kumbur [b], Ying Sun [a,*]

[a] *Complex Fluids and Multiphase Transport Laboratory, Department of Mechanical Engineering and Mechanics Drexel University, Philadelphia, PA 19104, USA*
[b] *Electrochemical Energy Systems Laboratory, Department of Mechanical Engineering and Mechanics Drexel University, Philadelphia, PA 19104, USA*

ARTICLE INFO

ABSTRACT

The vanadium redox flow battery (VRFB) has emerged as a viable grid-scale energy storage technology that offers cost-effective energy storage solutions for renewable energy applications. In this paper, a novel methodology is introduced for modeling of the transport mechanisms of electrolyte flow, species and charge in the VRFB at the pore scale of the electrodes; that is, at the level where individual carbon fiber geometry and electrolyte flow are directly resolved. The detailed geometry of the electrode is obtained using X-ray computed tomography (XCT) and calibrated against experimentally determined pore-scale characteristics (e.g., pore and fiber diameter, porosity, and surface area). The processed XCT data is then used as geometry input for modeling of the electrochemical processes in the VRFB. The flow of electrolyte through the pore space is modeled using the lattice Boltzmann method (LBM) while the finite volume method (FVM) is used to solve the coupled species and charge transport and predict the performance of the VRFB under various conditions. An electrochemical model using the Butler–Volmer equations is used to provide species and charge coupling at the surfaces of the carbon fibers. Results are obtained for the cell potential distribution, as well as local concentration, overpotential and current density profiles under galvanostatic discharge conditions. The cell performance is investigated as a function of the electrolyte flow rate and external drawing current. The model developed here provides a useful tool for building the structure–property–performance relationship of VRFB electrodes.

© 2011 Elsevier Ltd. All rights reserved.

1. Introduction

The vanadium redox flow battery (VRFB) was pioneered in the 1980s by Skyllas-Kazacos and co-workers [1–3] as a means to facilitate energy storage and delivery from intermittent energy sources like wind and solar power systems. The intention was to use the VRFBs as rechargeable batteries which can be charged or discharged depending on whether energy is required to be stored or utilized. A simplified schematic of a VRFB is shown in Fig. 1. At its core, the VRFB consists of two porous electrodes separated by an ion exchange membrane. An electrolyte consisting of vanadium ions dissolved in a sulfuric acid (H_2SO_4) solution flows through the porous electrodes. The V^{3+} and V^{2+} ions are present in the negative electrolyte, while the VO_2^+ and VO^{2+} ions are present in the positive electrolyte. The electrodes are composed of carbon fibers and form an electrically conductive fibrous network as depicted in Fig. 1. The pore space between the carbon fibers allows for flow of the electrolyte, while the surface of the fibers facilitates the electrochemical reactions. During the discharging cycle, the following reactions take place at the surface of the carbon fibers

Negative half cell : $V^{2+} \rightarrow V^{3+} + e^-$ (1)

Positive half cell : $VO_2^+ + 2H^+ + e^- \rightarrow VO^{2+} + H_2O$ (2)
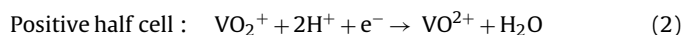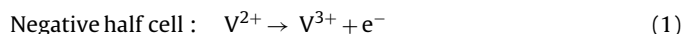
In the negative half cell, V^{2+} ions near the carbon fiber surface are oxidized and converted to V^{3+} ions. The free electrons generated at the carbon fiber surface travel through the conductive fibers to the current collector on the negative side, flow through the external circuit and enter the current collector on the positive side. The electrons then pass through the carbon fibers until they reach the fiber–electrolyte interface and combine with VO_2^+ ions to produce VO^{2+}. Catalysts are not necessary to initiate the reactions at either electrode. Based on the Gibbs free energy of the electrochemical reactions, the open circuit voltage (OCV) for reaction (1) is $E_n^0 = -0.255\,V$ [4] and that for reaction (2) is $E_p^0 = 0.991\,V$ [5], leading to a theoretical standard cell OCV of 1.246 V at a temperature $T = 298\,K$. Here, the subscripts n and p denote negative and positive, respectively.

A constant supply of V^{2+} ions and VO_2^+ ions, dissolved in sulfuric acid, is provided to the negative and positive electrodes, respectively, via pumps connected to external storage tanks (shown in

* Corresponding author. Tel.: +1 215 895 1373; fax: +1 215 895 1478.
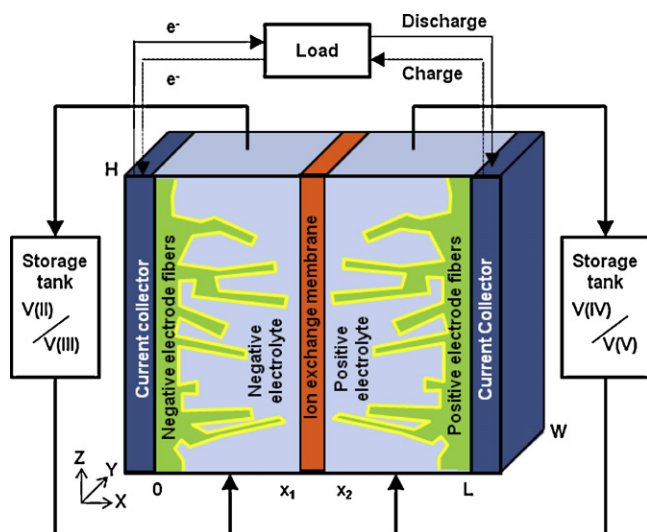 *E-mail address:* ysun@coe.drexel.edu (Y. Sun).

Fig. 1. Simplified schematic of a vanadium redox flow battery. In the present study, the solid electrode and liquid electrolyte phases are explicitly distinguished in the simulation geometry.

Fig. 1). The spent electrolyte then flows back to these storage tanks on both half cells. The battery can continue producing power as long as fresh reactants are available from the external storage tanks. An important consequence of these reactions is the migration of H^+ ions across the proton-conducting membrane from the negative half cell to the positive half cell in order to complete reaction (2) and to satisfy electroneutrality. The power rating of the VRFB depends on the active surface area available for the electrochemical reactions while the energy storage capacity is a function of the size of the storage tanks and the electrolyte composition within these tanks. If the VRFB is to be used as an energy storage device, the electrochemical processes described in Eqs. (1) and (2) above, operate in reverse, driven by an externally supplied potential which is used to recharge the solutions in the electrolyte tanks. Note that the pumps operate in the same direction, irrespective of the charging or discharging cycle of the VRFB. Although the VRFB appears similar in some respects to fuel cells, the main difference is that the electrolyte is in the form of a re-circulating liquid and changes its composition (ionic species concentration) during operation. For this reason, it is more appropriate to name this device as a rechargeable battery instead of a fuel cell [6].

Only a handful of numerical models [7–12] have been developed for the VRFB so far. These models can be classified as *macroscopic* or *volumetric* models in the sense that they use representative, volume-averaged structures and effective properties to develop their results. For example, the porous electrode is treated as a continuum for modeling purposes and the porosity and tortuosity values are used to calculate the effective transport properties through the electrode. Similarly, the active surface area available for electrochemical reactions is not based on measurements of the actual electrode geometry and very little or no details are provided about how these parameters are obtained. As a result, most macroscopic models cannot be used to examine the precise roles of the electrode microstructure and electrolyte flow configuration on the performance of the VRFB. In contrast to the existing macroscopic models, a novel methodology is proposed here to directly resolve the important species/charge/fluid transport processes at the electrode pore scale and meanwhile simulate the performance of VRFB at the system level. As expected, this approach is computationally expensive, but the advantage is that one can correlate the performance of the VRFB to the exact electrode

microstructure and electrolyte flow configuration, and thus be able to optimize the microstructure to improve the system-level performance. A similar *pore-scale* approach has led to promising results for solid oxide fuel cells (SOFCs) [13–17] and polymer electrolyte membrane (PEM) fuel cells [18–20], although to the best of authors' knowledge the integration of transport processes and electrochemistry within a single model has not been achieved as of yet for either a SOFC or a PEM fuel cell using a pore-scale approach. The present model of the VRFB accounts for coupled species/charge/fluid transport processes as well as electrochemistry, and the methodology presented herein can be applied to many electrochemical systems. The widespread availability of supercomputers has made the development of pore-scale transport resolved models feasible and numerical simulations can thus correspond more closely to the physics of the VRFB.

The remaining part of this paper is organized as follows. Section 2 describes the procedure in acquiring and characterizing a reconstruction of the detailed, 3-D geometry of an actual VRFB electrode material using X-ray computed tomography (XCT). The pore-scale model assumptions and governing equations for various transport processes taking place in the electrode are discussed in Section 3. Implementation details about the lattice Boltzmann method (used to simulate the flow of electrolyte) and the finite volume method (for charge and species transport) are provided in Section 4. Model results are presented and discussed in Section 5 followed by conclusions and recommendations for further study in Section 6.

2. Microstructure characterization

A critical step in understanding the pore-scale transport phenomena in VRFBs is to acquire precise microstructural information of the porous graphite felt electrodes. This is obtained by imaging a commercial carbon-felt electrode material using X-ray computed tomography, pre-processing the resulting tomogram to minimize imaging errors and then digitally assembling it into a virtual volume, and finally characterizing the 3-D geometry to determine the phase connectivity, porosity, feature size distributions, and specific surface area.

2.1. X-ray computed tomography

X-ray computed tomography (XCT) is a non-destructive imaging and metrology technique used to acquire precise microstructural reconstructions with sub-micron resolution. The sample attenuates the X-ray signal according to the local material density, providing excellent contrast of distinct phases of dissimilar density (e.g., carbon fiber and pore/void phases). A sample of Electrolytica GFS6-3mm carbon felt (typically used in VRFBs) is imaged using a SkyScan 1172 X-ray tomograph. Preliminary analysis of the material using scanning electron microscopy (SEM) and XCT revealed pore and fiber sizes approximately ranging from 20 to 200 μm and 10 to 80 μm, respectively (Fig. 2). A resolution of 1.5 μm is chosen to ensure ample identification of geometric features while still providing a large and representative domain for analysis.

To distinguish (segment) the carbon fiber and pore phases in the grayscale XCT tomogram, a binary segmentation procedure is performed based on a pixel intensity threshold chosen such that the resulting dataset matches the porosity experimentally obtained via mercury intrusion porosimetry (i.e., 92.6%). The resulting binary tomogram is then assembled into a three-dimensional (3-D) digital array, where each entry corresponds to a 1.5 μm × 1.5 μm × 1.5 μm voxel belonging to either the pore phase (0) or the fiber phase (1). The resulting virtual volume array (or a
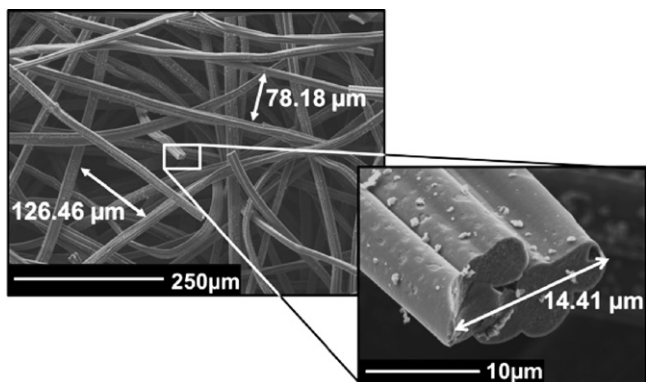
Fig. 2. SEM micrographs used to determine the characteristic length scales of the electrode material. These characteristic length scales are considered when selecting a resolution for the XCT imaging.

subset of it) can then be used as a geometric input into the pore-scale resolved transport model, as shown in Fig. 3.

2.2. Transport property analyses

The virtual volume generated for the tested electrode sample is directly analyzed to determine key transport metrics such as phase connectivity, porosity, pore size distribution, and active surface area. Traditional porometric techniques (mercury intrusion, liquid extrusion, etc.) utilize differential pressure to force a fluid through a sample. The mechanical interactions caused by the pressurized fluid can alter or damage the microstructure of the sample, resulting in metrics which are not representative of a virgin sample. The XCT-based approach described here, however, avoids these inaccuracies by directly analyzing the microstructure-sensitive properties of the virgin sample, without the use of secondary measurements such as differential pressure. The details of each microstructural property analysis are explained below, and the results for a 1.5 mm × 1.5 mm × 1.5 mm carbon-felt sample are tabulated in Table 1. The method used here is also applicable for characterizing other porous materials.

2.2.1. Porosity, internal surface area, and pore-size distribution

Porosity and internal (active) surface area are key geometric parameters that characterize the porous electrode material, and can be readily obtained from the XCT-reconstructed virtual volume. Porosity is defined as the fraction of the total sample volume which is occupied by the pore phase, and can be obtained by counting the number of voxels belonging to each respective phase. Internal surface area is characterized at all locations where the pore phase interfaces with the fiber phase. In computing internal surface area, the face-connected neighbors of every fiber-phase voxel in the volume are checked. If a neighbor is a pore-phase voxel, then the shared face is counted toward the internal surface area.

Both pore and fiber size distributions for the sample are obtained according to the following algorithm: features (pores or fibers) of a given size are removed from the dataset by performing a morphological opening operation. The opening operation utilizes a structuring element template to identify features of a specific size and shape. The change in phase volume due to the opening operation provides an indication of the prevalence of features which fit the structuring element. A distribution is obtained by tracking the change in phase volume while iterating the opening operation with structuring elements of increasing size. The resulting pore and fiber size distributions and a schematic of the operation is shown in Fig. 4. In this study, a circular structuring element with a diameter varying from 7.34 μm to 588.62 μm is used.

2.2.2. Phase connectivity

Phase connectivity is a crucial parameter for pore scale modeling. For instance, electrolyte flow and species transport can only occur through the connected pore region, while electron transport can only occur through the connected fiber region. Disconnected phases manifest themselves as floating islands of material and play no part in the electrochemical simulation. In this study, a face-connected criterion is utilized, i.e., voxels of the same phase must share a common face to be considered connected, while phases sharing only a common edge or corner are not considered connected. Connectivity is hence defined relative to the current collector for the solid electrode phase, and relative to the cell inlet (i.e., the inlet of electrolyte flow at the bottom of each half cell) for the liquid electrolyte phase. An algorithm can be employed in which a connectivity marker (or a colored dye) is injected from the appropriate reference plane into the phase of interest and is allowed to permeate throughout the volume, marking connected phases as defined by the face-connectivity criterion. Once this process is complete, disconnected phases can be readily identified, and removed.
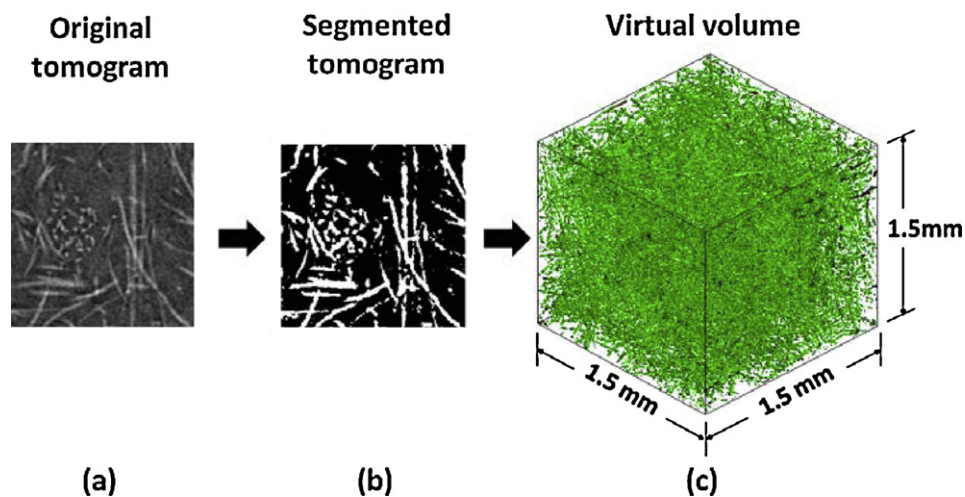

Fig. 3. Procedure for reconstructing microstructural electrode fiber virtual volume using XCT. (a) A tomogram is generated by imaging the electrode material at high resolution. (b) The tomogram is then segmented to distinguish the carbon fibers from the pores. (c) Finally, the binary images are stacked together and reconstructed into a virtual volume for further analysis. The original "master" dataset for the fiber structure is comprised of 1000 × 1000 × 1000 voxels at 1.5 μm/pixel resolution.

Table 1
Characterization of XCT reconstructed carbon-felt geometry.

	Units	XCT subset	XCT master	Experimental
Lattice size [x,y,z]	voxels	$120 \times 30 \times 120$	$1000 \times 1000 \times 1000$	–
Grid resolution	μm/voxel	4.5	1.5	–
Cell dimensions [L,W,H]	mm	$0.6 \times 0.15 \times 0.6$	$1.5 \times 1.5 \times 1.5$	–
Porosity	–	0.9129	0.9256	0.9260[a]
Specific surface area	mm^2/mm^3	39.7	41.9	37.5[a]
Mean pore diameter	μm	137.2	115.5	102.2 ± 8.27[a]
Mean fiber diameter	μm	17.26	15.16	20.80 ± 6.53[b]

[a] Obtained from mercury intrusion.
[b] Obtained from SEM imaging.

2.3. Simulation geometry

The last step in the construction of the simulation geometry is the utilization of the XCT fiber structure. To make the simulation dataset more computationally feasible, the input structure is limited to a few hundred thousand elements (the 1.5 mm $\times$ 1.5 mm $\times$ 1.5 mm master structure alone consists of 1 billion node points). The following measures are taken in order to produce a simulation geometry that offers a good representation of the master structure and is computationally feasible. First, a smaller geometric subset of the original master XCT structure must be extracted. Care is taken to ensure that the smaller subset exhibits the same geometric properties as the original master. Four parameters are selected as points of comparison between the subset and master geometry: surface area, porosity, pore size distribution, and fiber size distribution. An algorithm is then employed to check these parameters for every subset in the master geometry. The

subset fiber structures are free of disconnected phases as defined by the face connectivity criterion. The one with the lowest weighted error is selected as the optimal subset for use as an input geometry for the pore-scale resolved transport model. Second, the resolution of the subset geometry is coarsened to 3 times that of the original XCT data, from 1.5 μm/pixel to 4.5 μm/pixel. This is done by marching through the original high-resolution geometry and collecting multiple nodes in a $3 \times 3 \times 3$ control volume, in which the phase of majority contained in the volume will be assigned to a new low-resolution geometry to represent the same physical structures of the high-resolution geometry.

Fig. 5 shows the 3-D simulation geometry with all the major components of the flow cell. The optimal fiber subset taken from the original XCT master structure is duplicated in both half cells. The entire simulation geometry is comprised of $120 \times 30 \times 120$ voxels. The geometric parameters for the subset geometry as well as the original master are tabulated in Table 1. As shown in the same
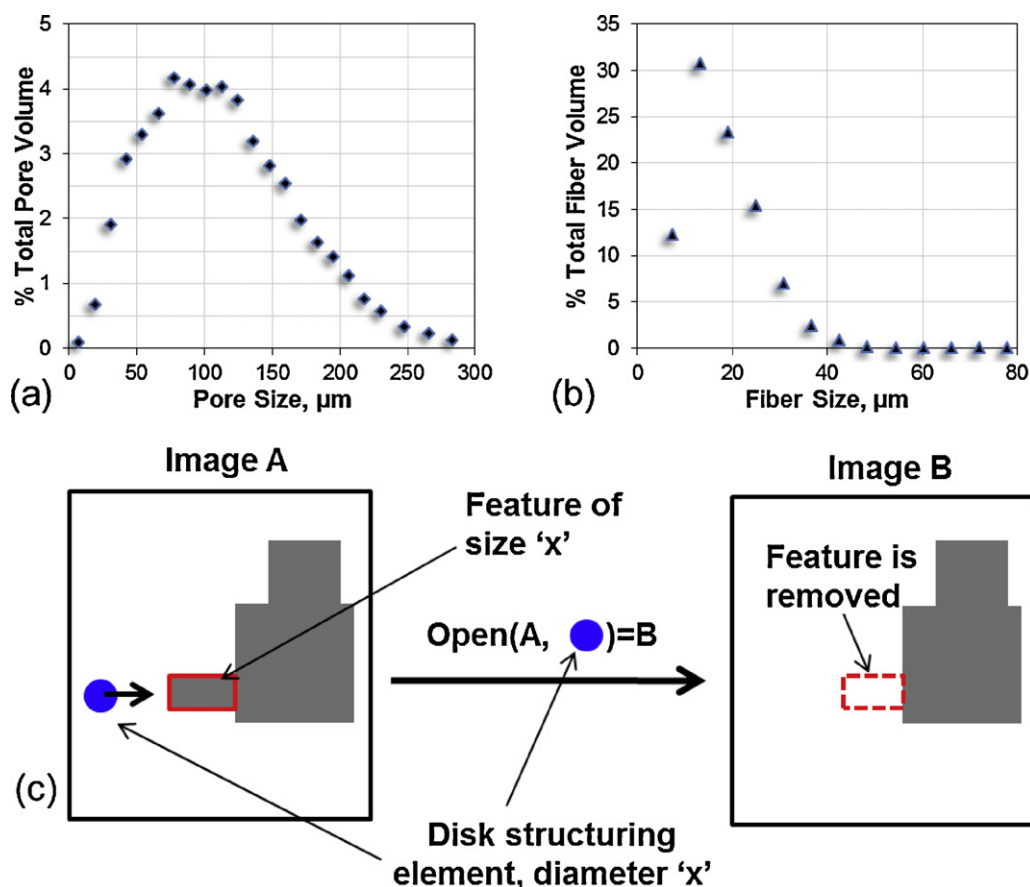

Fig. 4. The pore (a) and fiber (b) size distributions for the sample material. To obtain these distributions, the morphological opening operator is used in conjunction with a disk-shaped structuring element to identify and remove structures of size 'x' (c). The distribution function is determined by the difference in volume between the original and final datasets (images A and B, respectively). The complete distribution is obtained by iterating the process using structuring elements of increasing size.
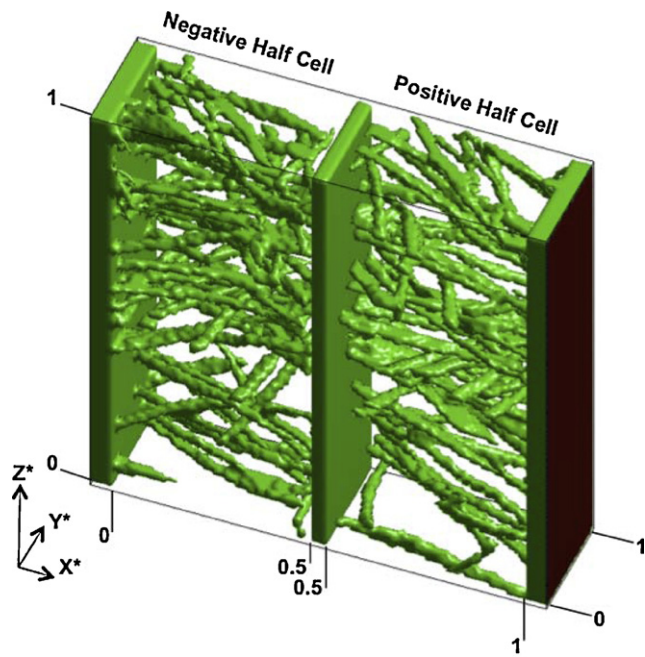
Fig. 5. Simulation geometry used in the 3-D pore-scale simulation. The fiber structure used in the geometry is a subset taken from the original master XCT geometry and exhibits an optimal match of geometric parameters.

figure, a convention of dimensionless length, width, and height (X^*, Y^*, Z^*, respectively) will be used throughout this paper. Note that X^* is only defined relative to the total length of the positive and negative half cells between the current collector and membrane, and a discontinuity exists in X^* across the membrane, i.e., $X^* = X/[(x_1) + (L - x_2)]$ where $0 \leq X \leq x_1$ or $x_2 \leq X \leq L$. Y^* and Z^* are defined relative to the total cell width and height, respectively, based on $Y^* = Y/W$ and $Z^* = Z/H$. Additionally, unless otherwise noted, the negative half cell will always be shown on the left, and vice versa for the positive half cell.

3. Model assumptions and equations

Having obtained a detailed reconstruction of the carbon-felt geometry, pore-level transport models were developed to simulate the flow of electrolyte, the transport of ionic species (reactants and products), the charge transport (electric current) through both the solid and the liquid phases, as well as the electrochemical reactions at the carbon fiber surface.

3.1. Fluid transport

The flow of liquid electrolyte through the connected pore space is governed by the continuity equation and the Navier–Stokes equations given by

$$\nabla \cdot \mathbf{u} = 0 \tag{3}$$

$$\frac{\partial \mathbf{u}}{\partial t} + (\mathbf{u} \cdot \nabla)\mathbf{u} = -\frac{1}{\rho}\nabla p + \nu \nabla^2 \mathbf{u} \tag{4}$$

where $\mathbf{u}$ is the liquid (electrolyte) velocity, ρ is the density, p is the pressure and ν is the kinematic viscosity. In lieu of the traditional computational fluid dynamics (CFD) approach to modeling the above set of equations, the lattice Boltzmann method (LBM) will be utilized in this study. The LBM has been well established as an efficient alternative to solving the Navier–Stokes equations in complex geometries such as flow in porous media. In this study,

Table 2
Species transport parameters.

Species	Concentration (C_j)	Charge (z_j)	Diffusivity (m² s⁻¹)
V²⁺	C_{II}	+2	2.4×10^{-10} [10]
V³⁺	C_{III}	+3	2.4×10^{-10} [10]
VO²⁺	C_{IV}	+1	3.9×10^{-10} [10]
VO₂⁺	C_V	+2	3.9×10^{-10} [10]
H⁺	C_{H^+}	+1	9.312×10^{-9} [12]
H₂O	C_{H_2O}	0	2.3×10^{-9} [10]
SO₄²⁻	$C_{SO_4^{2-}}$	−2	2.2×10^{-10} [10]

the following assumptions are made for modeling the flow of electrolyte:

- The electrolyte is incompressible and Newtonian.
- The viscosity is uniform throughout the electrode.
- The ionic species do not influence the flow field in any manner.
- No-slip boundary conditions are assumed to hold at the carbon fiber surface.
- The flow is driven by a constant pressure gradient along the Z-axis.
- Isolated pores do not contain liquid electrolyte and ionic species.

3.2. Species transport

Let the concentration of species j be represented by C_j, $j \in \{$II, III, IV, V, H⁺, H₂O$\}$, where the first four numerals denote the charge of vanadium species (II corresponds to V(II), etc.). The transport of species j within the electrolyte (flowing through the pores) is governed by the convection–diffusion equation, with an additional term to account for electrokinetic transport of charged species:

$$\frac{\partial C_j}{\partial t} + \mathbf{u} \cdot \nabla C_j = D_j \nabla^2 C_j + \nabla \cdot \left[\frac{z_j C_j D_j}{RT} \nabla \phi \right] \tag{5}$$

where D_j is the diffusivity of species j, z_j is the charge of species j, R the universal gas constant, T the absolute temperature, and ϕ the electrical potential. The concentration of SO₄²⁻ is obtained via the *electroneutrality* condition, $\sum z_j C_j = 0$. It should be noted that the electrokinetic transport term, the last term on the right-hand side of Eq. (5), is neglected in this present study, because its effect is negligible in redox flow batteries [12]. In the ion-exchange membrane, H⁺ is assumed to be the only active species. Assuming the membrane is fully saturated, the concentration of H⁺ is equivalent to the amount of fixed charged sites C_f in the membrane structure, which for a Nafion® membrane correlates to the concentration of sulfonic acid groups [10]. The values of the species-dependent parameters are given in Table 2. The following assumptions are made regarding the transport of ionic species in the present model:

- The concentration of all ionic species within the solution is very dilute.
- The effects of species cross-over in the membrane are negligible.
- The sulfuric acid completely dissociates into sulfate SO₄²⁻ and protons H⁺.
- The species do not interact with each other in the bulk fluid and the only diffusivity that matters is the diffusivity of the species in the solvent.
- Migration of H⁺ and H₂O across the ion-exchange membrane is neglected.

3.3. Charge transport

Inside the solid carbon fibers, the current density $\mathbf{J}$ is calculated via

$$\mathbf{J} = -\kappa_s \nabla \phi \tag{6}$$

Table 3
Charge transport parameters.

Description	Symbol	Value	Units
Solid conductivity	κ_s	1000	S m^{-1}[a]
Electrolyte conductivity	κ_{eff}	Eq. (8)	S m^{-1}
Membrane conductivity	κ_{mem}	Eq. (8)	S m^{-1}
External current density	J_{ext}	400	A m^{-2}

[a] Estimated.

Table 4
Parameters used in the Butler–Volmer equation.

Description	Symbol	Value	Units
Anodic transfer coefficient: negative	$\alpha_{1,a}$	0.5[a]	–
Cathodic transfer coefficient: negative	$\alpha_{1,c}$	0.5[a]	–
Anodic transfer coefficient: positive	$\alpha_{2,a}$	0.5[a]	–
Cathodic transfer coefficient: positive	$\alpha_{2,c}$	0.5[a]	–
Standard reaction rate constant: negative	k_1	1.7×10^{-7} [3]	m s^{-1}
Standard reaction rate constant: positive	k_2	6.8×10^{-7} [23]	m s^{-1}
Equilibrium potential: negative	E_2^0	0.991 [5]	V
Equilibrium potential: positive	E_1^0	−0.255 [4]	V
Operating temperature	T	298	K

[a] Estimated.

where κ_s is the electrical conductivity of the solid fibers. Because charge is conserved, the current density field is divergence free ($\nabla \cdot \mathbf{J} = 0$) and the governing equation for the potential field can be written as

$$\nabla \cdot (\kappa_s \nabla \phi) = 0 \tag{7}$$

In the electrolyte occupying the pore space, the effective electrical conductivity κ_{eff} is defined using

$$\kappa_{eff} = \frac{F^2}{RT} \sum z_j^2 D_j C_j \tag{8}$$

and the potential field is obtained via

$$\nabla \cdot \left[\kappa_{eff} \nabla \phi + F \sum z_j D_j \nabla C_j \right] = 0 \tag{9}$$

where F is Faraday's constant ($F = 96{,}485 \, \text{C mol}^{-1}$). For this study, Eqs. (8) and (9) are also applied to solve the potential within the ion-exchange membrane. The default values of these parameters are summarized in Table 3.

3.4. Boundary and initial conditions

3.4.1. Electrochemical reactions at the active surface

The rate at which species are generated or consumed at electrode–electrolyte active surfaces depends on their local concentrations in the proximity of the electrode fibers. In contrast to a volume-averaged approach, the species concentrations at the active surface (C_j^s) are directly available in the current pore-scale model. In this work, the Butler–Volmer equations are employed to couple the species concentrations at the active surface (represented by the superscript s) to the electrical potential in the solid and liquid phases across the active surface. During discharge, the mole fluxes for V^{2+} and V^{3+} in the negative half cell are denoted by $\mathbf{N}_{II}$ and $\mathbf{N}_{III}$, respectively, and are calculated using

$$-\mathbf{N}_{II} \cdot \hat{\mathbf{n}} = \mathbf{N}_{III} \cdot \hat{\mathbf{n}} = k_1 (C_{II}^s)^{\alpha_{1,c}} (C_{III}^s)^{\alpha_{1,a}} \left[\exp \left(\frac{\alpha_{1,a} F \eta_1}{RT} \right) \right.$$
$$\left. - \exp \left(-\frac{\alpha_{1,c} F \eta_1}{RT} \right) \right] \tag{10a}$$

where $k_1 (C_{II}^s)^{\alpha_{1,c}} (C_{III}^s)^{\alpha_{1,a}}$ on the right-hand side of Eq. (10a) represents the *exchange current density* [6]. The unit normal on the surface of the carbon fiber, pointing from the solid into the electrolyte phase is denoted by $\hat{\mathbf{n}}$. On the positive half cell, the mole fluxes for VO$_2^+$ and VO^{2+} are denoted by $\mathbf{N}_V$ and $\mathbf{N}_{IV}$, respectively, and are calculated using

$$\mathbf{N}_{IV} \cdot \hat{\mathbf{n}} = -\mathbf{N}_V \cdot \hat{\mathbf{n}} = k_2 (C_{IV}^s)^{\alpha_{2,c}} (C_V^s)^{\alpha_{2,a}} \left[\exp \left(\frac{\alpha_{2,a} F \eta_2}{RT} \right) \right.$$
$$\left. - \exp \left(-\frac{\alpha_{2,c} F \eta_2}{RT} \right) \right] \tag{10b}$$

In the above equations, k_1 and k_2 are reaction rate constants for reactions (1) and (2), respectively, $\alpha_{i,a}$ and $\alpha_{i,c}$ are the anodic and cathodic transfer coefficients, where the subscript i denotes

reactions (1) and (2). The overpotentials at the negative and positive electrodes are denoted by η_1 and η_2 and are given by

$$\eta_1 = \phi_s - \phi_e - E_1 \tag{11}$$

$$\eta_2 = \phi_s - \phi_e - E_2 \tag{12}$$

where $\phi_s - \phi_e$ represents the voltage drop between the solid phase and the electrolyte. The effective voltages E_1 and E_2 on the respective electrodes are obtained using

$$E_1 = E_1^0 + \frac{RT}{F} \ln \left(\frac{C_{III}}{C_{II}} \right) \tag{13}$$

$$E_2 = E_2^0 + \frac{RT}{F} \ln \left(\frac{C_V}{C_{IV}} \right) \tag{14}$$

Eqs. (13) and (14) are the so-called Nernst equations that are used to calculate the effect of reactant and product concentrations on the open circuit voltage (OCV). For the VRFB, the OCV can be increased to 1.67 V by using high-purity vanadium solutions [21]. In addition, the relationship between the current density $\mathbf{J}$ and the species flux $\mathbf{N}$ is provided by Faraday's law

$$\mathbf{N} = \frac{\mathbf{J}}{F} \tag{15}$$

The parameter values used in the Butler–Volmer equations are summarized in Table 4.

3.4.2. Boundary conditions for mass and momentum balance

The flow of electrolyte takes place through the pore space of the electrode. At all fixed walls including the electrolyte/electrode and the electrolyte/membrane interfaces, a no-slip boundary condition is used. A zero gradient boundary condition is used at the domain walls at $Y^* = 0$ and $Y^* = 1$. The driving force for the electrolyte flow is a pressure difference and a high and a low fluid pressure are specified at the cell inlet ($Z^* = 0$) and outlet ($Z^* = 1$), respectively. The initial condition used for the velocity field is $\mathbf{u} = 0$.

3.4.3. Boundary conditions for species balance

For the quasi-steady-state simulation considered in this study (i.e., the storage tank is assumed to be very large), the change in inlet concentrations with time is negligible. Hence, in the electrolyte phase, Dirichlet concentration boundary conditions are specified for all species at the cell inlet ($Z^* = 0$) except sulfate. It is convenient to define the inlet concentration of any species (C_j^{in}) in terms of the total vanadium concentration of the positive ($C^{0,+}$) and negative ($C^{0,-}$) half cells and initial proton concentration of the initial positive ($C_{H^+}^{0,+}$) and negative ($C_{H^+}^{0,-}$) half cells with respect

Table 5
Total species concentrations.

Description	Symbol	Concentration (mol m^{-3})
Total vanadium concentration (positive electrode)	$C^{0,+}$	2000[a]
Total vanadium concentration (negative electrode)	$C^{0,-}$	2000[a]
Initial proton concentration (positive electrode)	$C_{H^+}^{0,+}$	4000[a]
Initial proton concentration (negative electrode)	$C_{H^+}^{0,-}$	6000[a]
Initial water concentration	$C_{H_2O}^0$	4200[b]
Fixed charge site concentration	C_f	1200 [22]

[a] Based on vanadium solubility limit.
[b] Estimated.

to the state of charge (SOC) of the electrolyte, as determined from

$$\text{SOC} = \frac{C_{II}}{C^{0,-}} = \frac{C_V}{C^{0,+}}$$

$$C_{II}^{in} = C^{0,-} \cdot \text{SOC}$$

$$C_{III}^{in} = C^{0,-} \cdot (1 - \text{SOC})$$

$$C_V^{in} = C^{0,+} \cdot \text{SOC} \qquad (16)$$

$$C_{IV}^{in} = C^{0,+} \cdot (1 - \text{SOC})$$

$$C_{H^+}^{in,-} = C_{H^+}^{0,-} + C^{0,-} \cdot \text{SOC}$$

$$C_{H^+}^{in,+} = C_{H^+}^{0,+} + C^{0,-} \cdot \text{SOC}$$

where the total vanadium and proton concentrations are given in Table 5. Unless otherwise stated, the SOC for all simulations is 50%. Outflow boundary conditions are used for all species in the electrolyte at the cell outlet at the top boundary ($Z^* = 1$).

At the electrode/electrolyte interface, the mole flux of electrochemically active species is calculated using the Butler–Volmer equation. For all other species, the flux at this interface is set to zero.

For the electrolyte/membrane interface, a zero-gradient flux boundary condition is imposed for all species, including H$^+$. To properly account for the transport of H$^+$ across the membrane, a simplified treatment to account for the bulk generation and depletion of H$^+$ in the electrolyte based on electroneutrality is adopted. As required by electroneutrality, during discharge, H$^+$ concentration decreases in the negative half cell and increases in the positive half cell by the same amount as protons migrate across the membrane. The change in H$^+$ concentration in the positive and negative electrolyte is hence accounted for by treating H$^+$ as a participant in the electrochemical reaction at the active surface of the carbon fibers. The bulk generation and depletion of H$^+$ in the positive and negative half cells, respectively, is then given by the positive and negative mole flux calculated in Eq. (10).

3.4.4. Boundary conditions for charge conservation

For the electric potential, a uniform external current density, J_{ext}, is applied on the current collector boundary at $X^* = 0$ and $-J_{ext}$ is applied at $X^* = 1$. The current density at the electrode/electrolyte interface is given by the Butler–Volmer equation. Zero potential

flux boundary conditions are imposed on all other surfaces of the simulation, including the cell inflow and outflow boundaries.

4. Solution methodology

The inputs to the numerical model are the domain geometry, physical properties of various parts of the battery, electrolyte flow conditions, species concentrations at the inlet, electrochemical reaction constants for the Butler–Volmer equations, transport coefficients for species and charge and the external current density at both negative and positive current collectors. Once these quantities are properly specified, the flow field inside the porous electrodes is calculated first using LBM. The coupled potential and species concentration fields are then simultaneously solved using an iterative method until a steady-state solution is obtained or until the desired charging and discharging behavior of the flow battery is simulated. Here, constant inlet concentrations are assumed, which essentially represent an unlimited supply of fresh ionic species from the storage tanks (assumed to be of infinite size) to both electrodes, at a rate determined by the pumping speed. One primary outcome of the numerical model is the potential difference across the negative and positive current collectors, i.e., the cell voltage. In the following subsections, the LBM for fluid flow and the finite volume method for coupled species and charge transport are discussed.

4.1. Lattice Boltzmann method (LBM) for fluid flow

Unlike the Navier–Stokes equations, where fluid velocity and pressure are the primary independent variables, the primary variables in the LBM are the particle velocity distribution functions (PDFs). The PDF at spatial location $\mathbf{x}$ along direction α is denoted by f_α and can be thought of as representing the number of fluid particles at location $\mathbf{x}$ that are moving along the direction α. The LBM simulates incompressible fluid flow by tracking the transport of these PDFs on a discrete Cartesian lattice, where the PDFs can only move along a finite number of directions corresponding to the neighboring lattice nodes. The particle velocities are such that PDFs jump from one lattice node to the neighboring lattice node in one time step. The lattice Boltzmann equation (LBE) describes the evolution of PDF populations (along a finite number of directions) with time at each lattice node

$$f_\alpha(\mathbf{x} + \mathbf{e}_\alpha, t+1) = f_\alpha(\mathbf{x}, t) - \left[\frac{f_\alpha(\mathbf{x}, t) - f_\alpha^{eq}[\rho(\mathbf{x}, t), \mathbf{u}(\mathbf{x}, t)]}{\tau} \right] \qquad (17)$$

The right hand side of Eq. (17) represents the collision process, where the effects of external forces and interactions of different PDFs arriving at node $\mathbf{x}$ from neighboring nodes is considered. The relaxation time τ controls the kinematic viscosity ν of the Boltzmann fluid via the relation

$$\nu = \frac{2\tau - 1}{6} \qquad (18)$$

The "post-collision" PDF then streams to the left hand side of Eq. (17). The 19 base velocities $\mathbf{e}_\alpha$ for the D3Q19 velocity model are given by

$$e_\alpha = \begin{bmatrix} 0 & 1 & -1 & 0 & 0 & 0 & 0 & 1 & -1 & -1 & 1 & 0 & 0 & 0 & 0 & 1 & -1 & -1 & 1 \\ 0 & 0 & 0 & 1 & -1 & 0 & 0 & 1 & 1 & -1 & -1 & 1 & -1 & -1 & 1 & 0 & 0 & 0 & 0 \\ 0 & 0 & 0 & 0 & 0 & 1 & -1 & 0 & 0 & 0 & 0 & 1 & 1 & -1 & -1 & 1 & 1 & -1 & -1 \end{bmatrix} \qquad (19)$$

where each column represents a base vector from the origin to the various neighboring node points ($\alpha = 0$–18).

Table 6
Weight factors used in the D3Q19 model.

$\alpha = 0$	$\alpha = 1, 2, 3, 4, 5, 6$	$\alpha = 7{-}18$
$w_\alpha = \frac{1}{3}$	$w_\alpha = \frac{1}{18}$	$w_\alpha = \frac{1}{36}$

The macroscopic density ρ and velocity $\mathbf{u}$ can be obtained at each lattice node by taking moments of f_α along all the discrete directions and are calculated using Eqs. (20) and (21)

$$\rho = \sum_{\alpha=0}^{18} f_\alpha \qquad (20)$$

$$\rho\mathbf{u} = \sum_{\alpha=1}^{18} f_\alpha e_\alpha \qquad (21)$$

The actual flow velocity $\mathbf{u}'$, used to plot velocity vector fields, is calculated using

$$2\rho\mathbf{u}' = \sum_{\alpha=1}^{18} f_\alpha \mathbf{e}_\alpha + \sum_{\alpha=1}^{18} f_\alpha^{eq}\mathbf{e}_\alpha \qquad (22)$$

The equilibrium distributions f_α^{eq} at each lattice node depend on the macroscopic density and velocity at that node and are given by

$$f_\alpha^{eq}(\rho, \mathbf{u}) = \rho w_\alpha \left[1 + 3(\mathbf{e}_\alpha \cdot \mathbf{u}) + \frac{9}{2}(\mathbf{e}_\alpha \cdot \mathbf{u})^2 - \frac{3}{2}(\mathbf{u} \cdot \mathbf{u})^2 \right] \qquad (23)$$

where the weight factors w_α are given in Table 6.

The presence of solid walls and inlets and outlets requires appropriate boundary conditions. The half-way bounce-back scheme [24–27] is used to model the no-slip boundary condition at the wall boundaries. To specify the fluid pressure at the inlet and outlet boundaries, the extrapolation scheme introduced by Guo et al. [28] is adopted here.

4.2. Finite volume method for charge and species transport

A three-dimensional finite-volume method (FVM) [29] has been used to solve the coupled charge and species transport equations in the porous electrode. The harmonic means of the diffusivity and/or

electrical conductivity are used for volumes whose faces represent the boundary between the liquid electrolyte, carbon fiber, and membrane. It is assumed that the surface concentrations in Eq. (10) (ideally at the faces of the control volume) can be approximated by the concentrations immediately adjacent to the surface. A fully implicit scheme and Jacobi method are applied to simultaneously update species and potential fields until a converged solution is obtained.

4.3. Solution procedure

As the first step of the pore-scale approach, LBM is used to calculate the flow field inside the porous carbon-felt electrode. The converged flow field obtained through LBM is in "lattice units," and must be converted to physical units via a matching Reynolds number

$$\left(\frac{U_{avg}L_{avg}}{\nu} \right)_{LBM\ units} = \left(\frac{U_{avg}L_{avg}}{\nu} \right)_{physical\ units} \qquad (24)$$

where the characteristic length scale, L_{avg}, is taken to be the average pore size based on the XCT data, and the characteristic velocity, U_{avg}, is defined as the average velocity of the cell inlet ($Z^* = 0$). Assuming that the kinematic viscosity of the electrolyte is similar to water ($\nu = 10^{-6}$ m^2 s^{-1}) and using the actual control volume size as the length scale ($\Delta x = 1$ in LBM units), one can calculate the scaling factor from the LBM-calculated velocity field to the correct velocity field in physical units throughout the pore-space of the carbon-felt electrode. For a given problem, the velocity field only depends on the geometrical details, fluid properties (viscosity) and on the pressure difference. Depending on the size of the solution domain along Z, a prescribed pressure difference between the inlet and outlet is specified such that Re = O(0.1), comparable to the values used in VRFB experiments and models [11]. The resulting flow field, in physical units is used in the FVM to solve for the coupled charge and species transport equations. A schematic of this methodology is shown on a 2-D cross section for a sample of a solid/pore network in Fig. 6.

The LBM and FVM methods were implemented in FORTRAN 90 using the Message Passing Interface (MPI) for parallel processing. The tolerance for potential and concentration fields was set to be
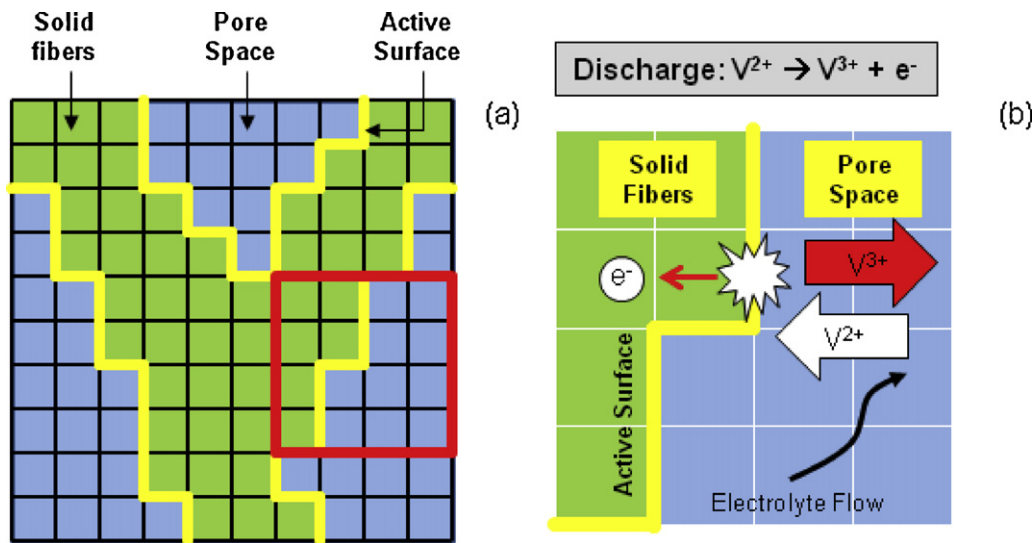

Fig. 6. Schematic of our pore-scale multiphase simulation geometry shown in a 2-D plane. (a) Solid fibers (green) and pore spaces (blue) are assembled in a Cartesian lattice, with the interface between the two phases (yellow line) signifying the active surface about which electrochemical reactions take place. (b) 4 × 4 subsection showing the electrochemical reaction occurring at an active surface for discharge of the negative half cell, which is modeled using the Butler–Volmer equation. The fluid transport in the pore phase is solved using the LBM, while the species and charge transport is solved using the FVM. (For interpretation of the references to color in this figure legend, the reader is referred to the web version of this article.)
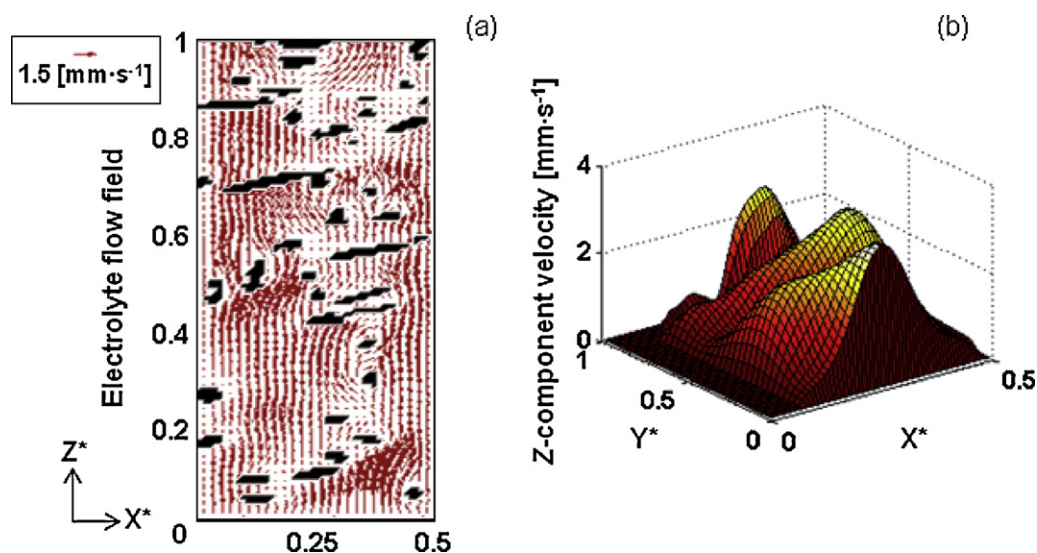
Fig. 7. LBM simulation of electrolyte flow through the porous carbon-felt electrode. (a) Velocity field in the negative half cell shown in cross section about the midplane in Y. (b) Vertical component of the fluid velocity in a XY plane at the inlet.

1×10^{-8}. A typical simulation based on a $120 \times 30 \times 120$ subset of the XCT structure converged with 20 h using a 64-core computer running on the TeraGrid.

5. Results and discussion

5.1. Flow through porous electrodes

For the baseline XCT simulation geometry, the LBM yielded an averaged inlet velocity of $U_{avg,LBM} = 9.938 \times 10^{-4}$. Using a LBM viscosity of $\nu_{LBM} = 1/6$ (which corresponds to a relaxation time of $\tau = 1$) and an averaged pore diameter of $L_{ave,LBM} = 30.4$ voxels (from Table 1) led to an Re = 0.182. The average inlet velocity was then found to be (utilizing Eq. (24)) $U_{avg,physical} = 1.325$ mm s^{-1}. Fig. 7 shows the Y-midplane velocity field and vertical component of inlet velocity in the negative half cell of the electrolyte flow through the porous electrode in physical units.

5.2. Effect of electrode surface area on cell voltage

A critical parameter in the operation of a flow battery is the active area available for electrochemical reactions at the surface of the carbon fibers. Simulations are conducted using idealized geometries of varying surface areas to investigate their effects on cell performance. Also, a simplified model derived from the basic principles of charge conservation is introduced to serve as an analytical utility in verifying and exploring the effects of surface area on cell performance.

5.2.1. Geometries for surface area analysis

Simple electrode geometries are used in order to examine the behavior of the system with respect to the active area available for electrochemical reactions. In Fig. 8, five idealized geometries of the flow battery are shown in XY-cross section (electrolyte flow is through the blue areas and coming out of the page) and all features shown are identical along the Z-axis. The objective is to successively increase the active area and to examine its effect on the cell voltage. A grid size of $120 \times 15 \times 20$ is used in all simulations with a 4.5 μm/pixel resolution so that the active areas of these simplified geometries vary on the order of 10^3–10^5 m^2/m^3.

5.2.2. Simplified model for calculating overpotentials and cell voltage of a VRFB

The detailed, pore-scale approach outlined in this paper is a general methodology for all parametric conditions. However, for a special range of problems, a simple method based on charge conservation can be used to predict the overpotentials and voltage drops in a VRFB for various operating parameters. The main assumptions and conditions under which this simplified model can be used are:

- The concentrations for all vanadium species do not change significantly from the values specified at the inlet to the electrodes.
- The VRFB is assumed to be operating at steady-state.
- Detailed geometric information regarding the active surface area of the porous electrode is available.
- Potential drops inside the solid phase, inside the liquid electrolyte and across the membrane are negligible compared to the potential drops across the active surfaces.
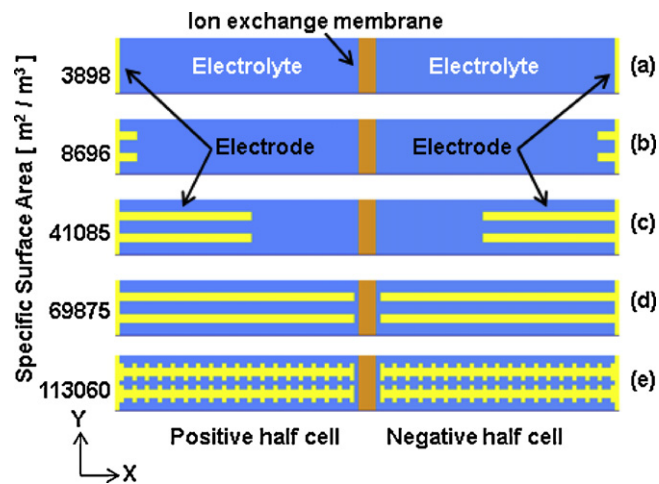

Fig. 8. Simplified electrode geometries used to examine the effect of specific area on the performance. Solid electrode and liquid electrolyte phases are denoted by yellow and blue, respectively (current collectors are not shown). Case (a) has the least active area. In cases (b), (c), and (d), the solid forms fin-like extensions into the liquid electrolyte. Case (e) shows fin structure with studded features to further increase surface area. (For interpretation of the references to color in this figure legend, the reader is referred to the web version of this article.)
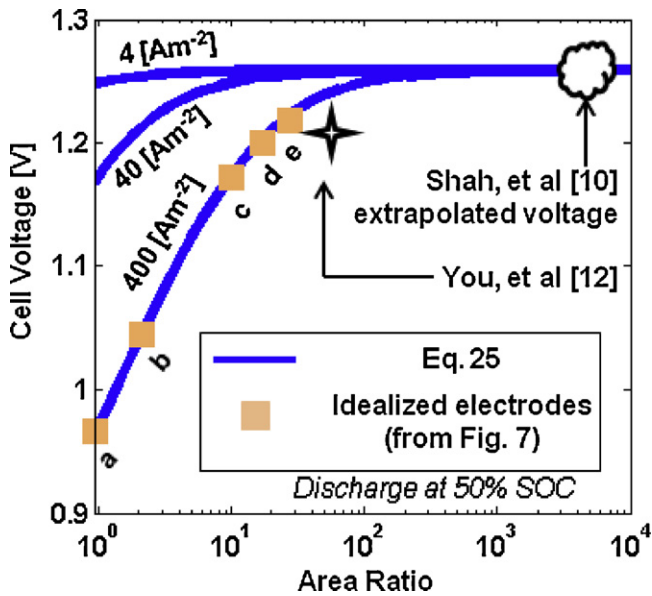
Fig. 9. Cell voltage against area ratio of the electrode for galvanostatic discharge at various current densities at 50% SOC. Charge conservation approximation of cell voltage agrees well with pore scale simulation results using idealized structures from Fig. 8 and XCT structure at discharge rate of 400 A m^{-2}. The reported cell voltage in You et al. [12] is within 1.8% of the simplified charge conservation model. A structure exhibiting area ratio used in Shah et al. [10] is expected to saturate at the open circuit potential if operating under the same conditions.

The basic idea of the simplified model is that at steady-state, the total current flowing in through the current collectors is exactly identical to the total current leaving/entering the active surface of the carbon fiber electrodes. If the surface area of the current collector is A_{ext} and the active area of the carbon fibers is A_1 and A_2 on the negative and positive electrodes, respectively, then

$$J_{ext}A_{ext} = \overline{J_1}A_1 = -\overline{J_2}A_2 \qquad (25)$$

where J_{ext} is the current density at the current collector, and $\overline{J_1}$ and $\overline{J_2}$ indicate the integrated average current densities over the negative and positive electrode surfaces, respectively. The ratio of the active surface area to the current collector area is defined as A^*. The area ratio A^* can also be expressed as the product of specific surface area (A/V, where V is the half cell volume) with the length, l, of the half cell via $A^* = A\,l/V$. If the length of the half cells remain constant (as is the present case), an increase in area ratio is equivalent to an increase in specific surface area.

Once the average current density at the active surface is known, one can estimate the average overpotential at the active surface using the Butler–Volmer equations of Eq. (10), assuming that the vanadium ion concentrations at the active surface are equal to the corresponding inlet concentrations. Based on these overpotential values, one can calculate the average potential drop across the active surface using Eqs. (11) and (12). Finally, the potential drops on the negative and positive side can be combined to obtain the operating voltage.

Because the height of our simulated batteries is small (on the order of tens of microns), no significant changes are expected in the species concentrations and the SOC remains almost identical to that present at the flow inlet boundary. Thus, this simplified model can be utilized in verifying our pore-scale simulated cell voltage.

5.2.3. Comparison between numerical results and simplified model

Fig. 9 shows the cell voltage as a function of the area ratio for several different discharge currents ranging from 0.4 to 400 A m^{-2} using the simplified charge conservation model of Eq. (25). The
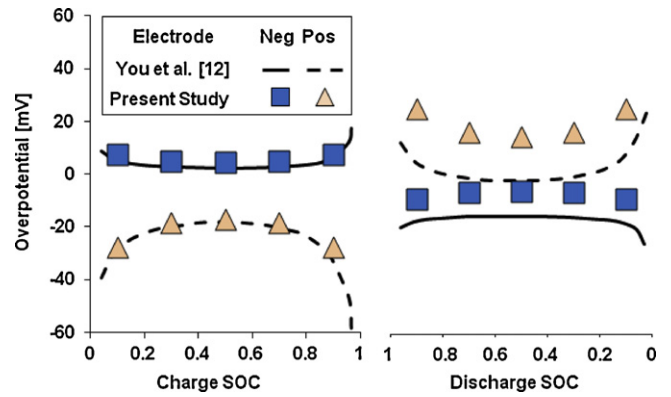

Fig. 10. Overpotential as a function of SOC compared against You et al. [12] under the same operating conditions with a galvanostatic current density of 400 A m^{-2}. As expected, the overpotentials for the pore-scale model in the present study are antisymmetric about SOC for each half cell between charging/discharging.

pore-scale simulations are carried out for a current density of 400 A m^{-2} and a SOC of 50%. It should be noted that to make comparison with the results of You et al. [12], the total vanadium concentration at the inlet of each electrode is set to be 2000 mol m^{-3}, the positive open circuit potential is set to 1.004 V, and the initial inlet hydrogen concentration is changed to 4500 mol m^{-3}.

Results from the idealized electrode geometries show good agreement with the model prediction. As shown in Fig. 9, an initial increase in cell voltage is observed with increasing surface area. This can be explained by the fact that with more surface area, the local current density at the active surface decreases, which decreases activation losses, resulting in a higher overall cell voltage. The cell voltage reported by You et al. [12] for the same current density is shown on the same figure and is within 1.8% of the value
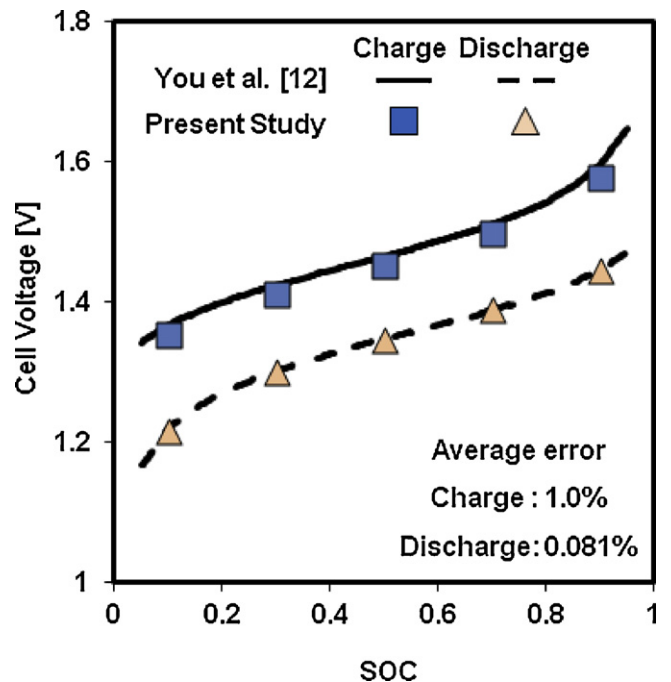

Fig. 11. Cell voltage as a function of SOC for pore scale model using idealized geometry compared against volumetric model results by You et al. [12] under the same operating conditions with a galvanostatic current density of 400 A m^{-2}. Excellent agreement indicates that the pore scale model is capable of reproducing results from volumetric models. Note that 140 mV has been added to the cell voltage of the pore scale results [12,30].
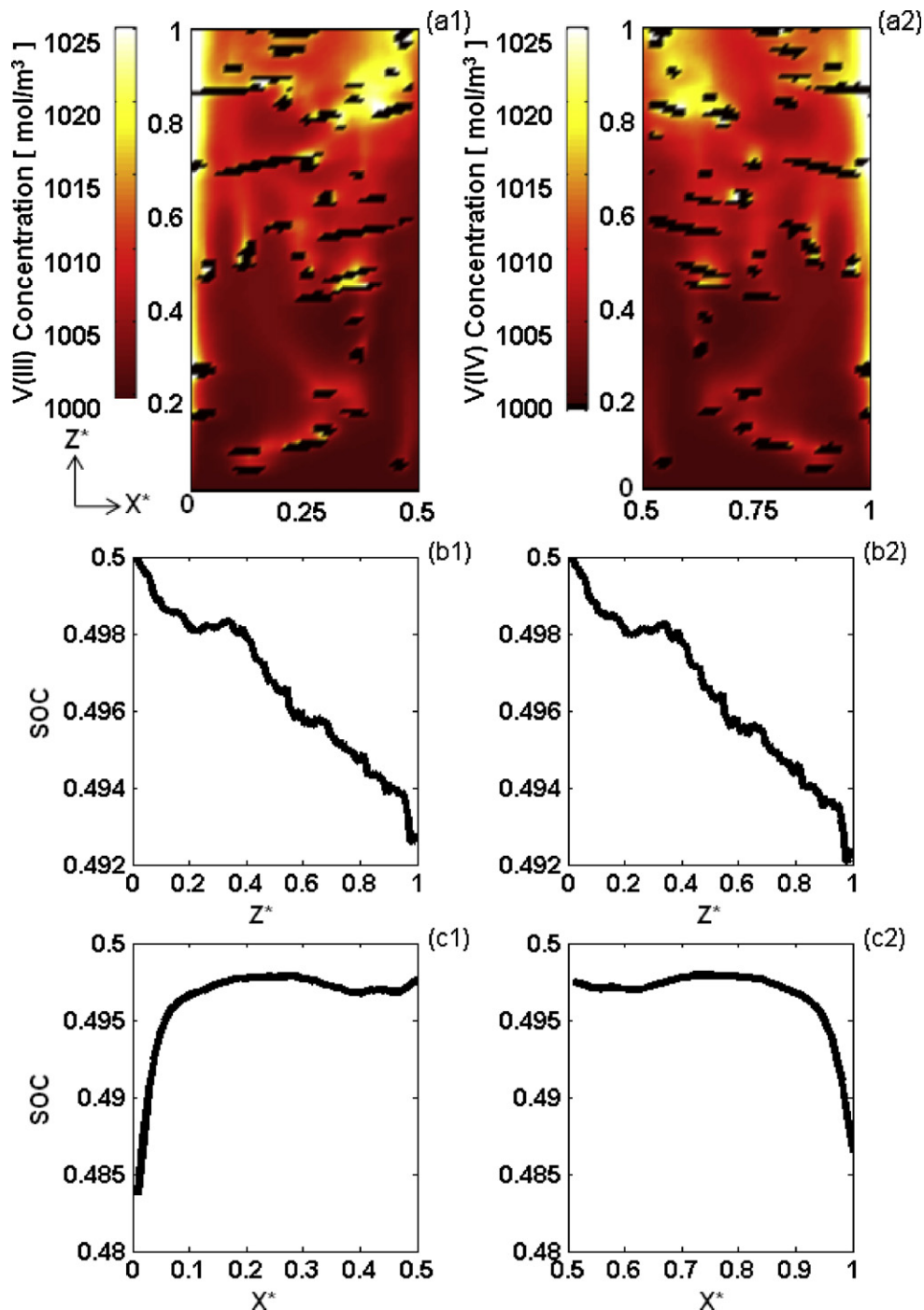
Fig. 12. Pore-scale predictions of concentration distribution in both half cells with an inlet SOC of 50% during galvanostatic discharge at 400 A m^{-2}. Distributions shown are (a) local concentration of V(III) and V(IV) at the Y-midplane, (b) corresponding averaged SOC along Z (where SOC fluctuations are due to local pore space variations in Z), (c) corresponding averaged SOC along X for both the (1) negative and the (2) positive half cells.

predicted by the simplified model. The discrepancy here is most likely due to the fact that the area ratio parameter does not properly account for the porosity.

From the simplified model, it can be seen that all cell voltages will tend to saturate at the open circuit voltage with an indefinite increase in area ratio. This represents the limiting case for flow cell operation at which there are essentially no losses from the electrode. However, the pumping requirements for utilizing such a densely packed electrode material would render such an electrode impractical. For comparison, the cell voltage as extrapolated from the large area ratio of Shah et al. [9] is shown on the figure and is expected to saturate at the open circuit voltage if operated under the same conditions as the present study. It is important to note that one must be cautious when extrapolating cell voltage from model predictions for large area ratios (but still smaller than the area ratio for full saturation) based on simplified charge conservation. This is because for large area ratios, species concentration may be impacted significantly, thereby invalidating the simplified charge conservation model. In contrast, the detailed pore-scale model can be applied for all specific area values.
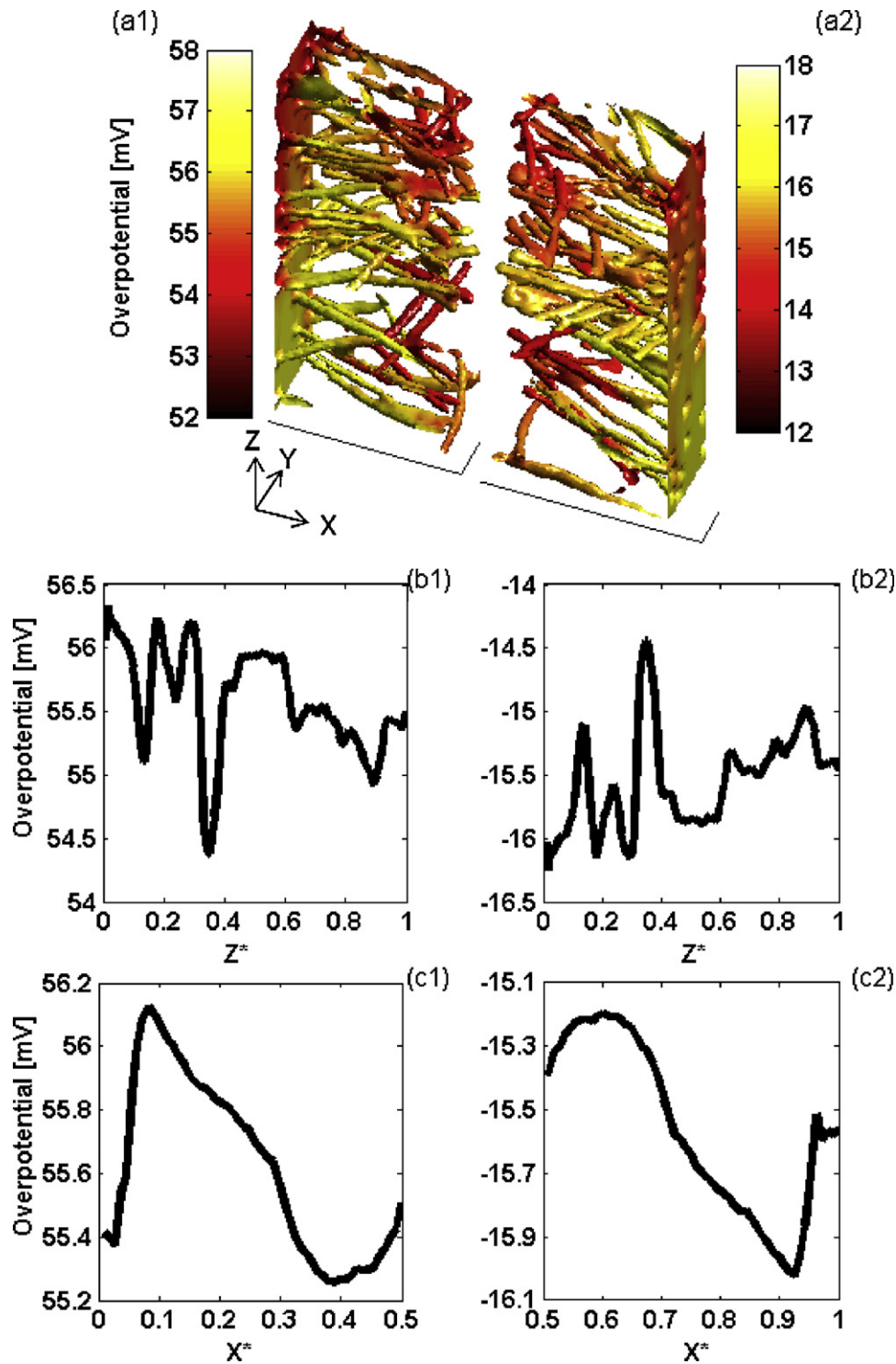
Fig. 13. Pore-scale predictions of overpotential distribution on the active surface with an inlet SOC of 50% during galvanostatic discharge at 400 A m^{-2}. Distributions shown are (a) local absolute value on the 3-D surface of the electrode fibers, (b) averaged along Z, (c) averaged along X for both the (1) negative and the (2) positive half cells.

5.3. Charging/discharging cycle

In this section, a quasi-steady state charging/discharging cycle of the flow cell is simulated using the pore-scale model based on steady-state solutions at different inlet SOCs assuming that an infinite supply of fuel is provided from the storage tank (or the storage tank is very large). The quasi-static cycling results are compared with those of You et al. based on a volume-averaged model [12]. A simplified fin geometry similar to that shown in Fig. 8e with an active area of 16,243 m^2/m^3, porosity of 91.6%, and half cell length of 3 mm is used to replicate the geometric parameters of the electrode material used by You et al. [12]. Furthermore, the total vanadium concentration at the inlet of each electrode is set to be 2000 mol m^{-3}, the positive open circuit potential is set to 1.004 V, and the initial inlet hydrogen concentration is changed to 4500 mol m^{-3}. With these modifications, the pore
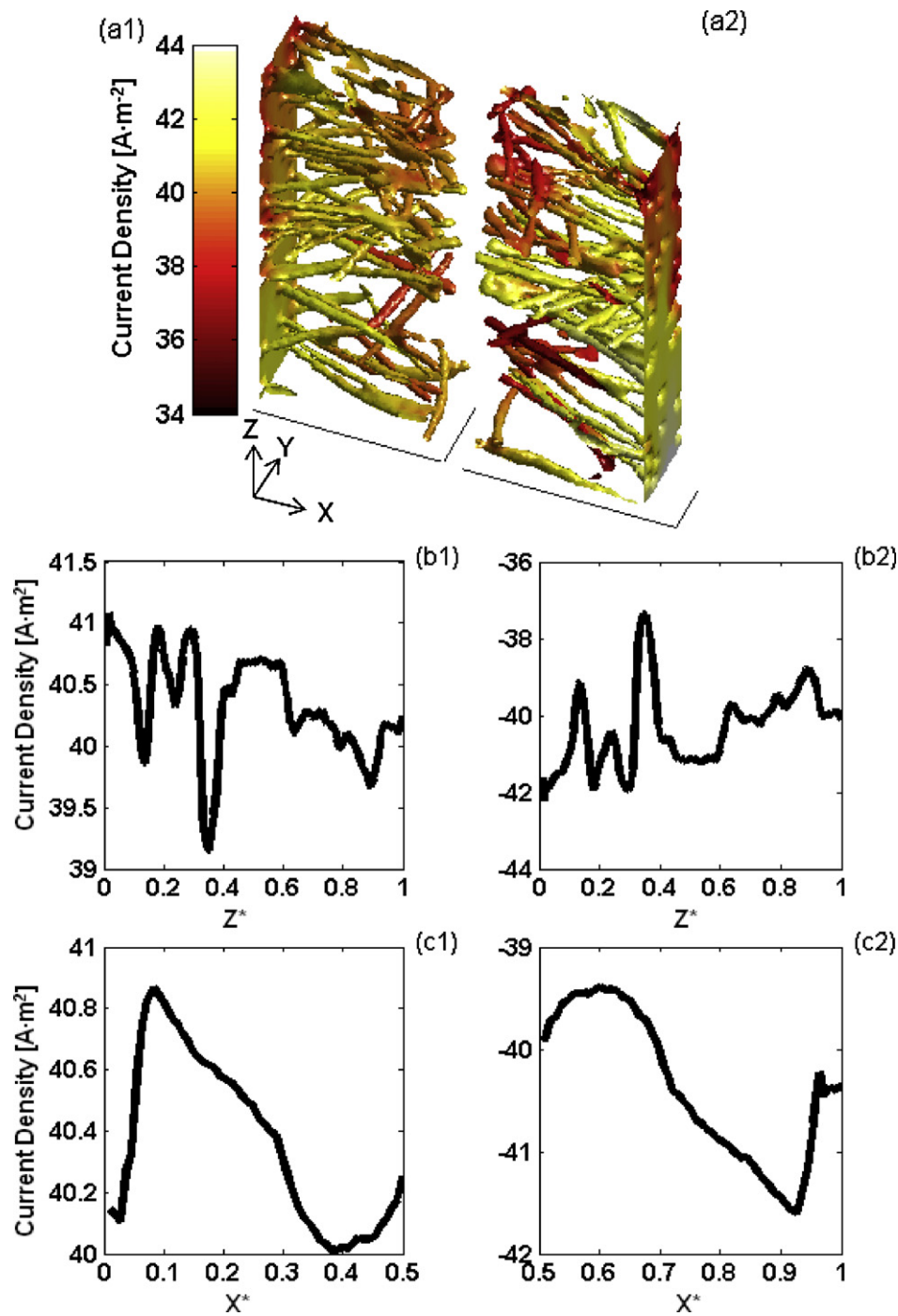
Fig. 14. Current density distribution on the active surface with an inlet SOC of 50% during galvanostatic discharge at 400 A m^{-2}. Distributions shown are (a) local absolute value on the 3-D surface of the electrode fibers (b) averaged along Z (c) averaged along X for both the (1) negative and the (2) positive half cells.

scale model parameters are now reminiscent of those used in You et al. [12].

The overpotentials physically represent the voltage drop across the electrode–electrolyte interface and depend on the operating conditions as well as the physical parameters used in the Butler–Volmer equation. Fig. 10 shows the integrated average of overpotentials over the entire active surface in each of the half cells during charging/discharging as compared to the results of You et al. [12]. It can be seen that the overpotentials match well for the charge cycle, but not for the discharge cycle. Since the only difference between the charging/discharging cycle is the polarity of the discharge current, it is expected that the distribution of the

overpotential is antisymmetric about SOC between the two discharge currents for each of the half cells. In other words, the overpotential of each of the half cells as a function of SOC will change signs if the polarity of the discharge current is reversed under the same operating conditions, which is what is observed with our pore scale results.

Fig. 11 shows the cell voltage during quasi-static charging/discharging for the pore-scale model as compared to the results of You et al. [12]. The average error between the results from the present study and the cell voltage calculated by You et al. [12] is 1.0% for the charge cycle and 0.081% for the discharge. The excellent agreement indicates that the pore-scale model is capable of
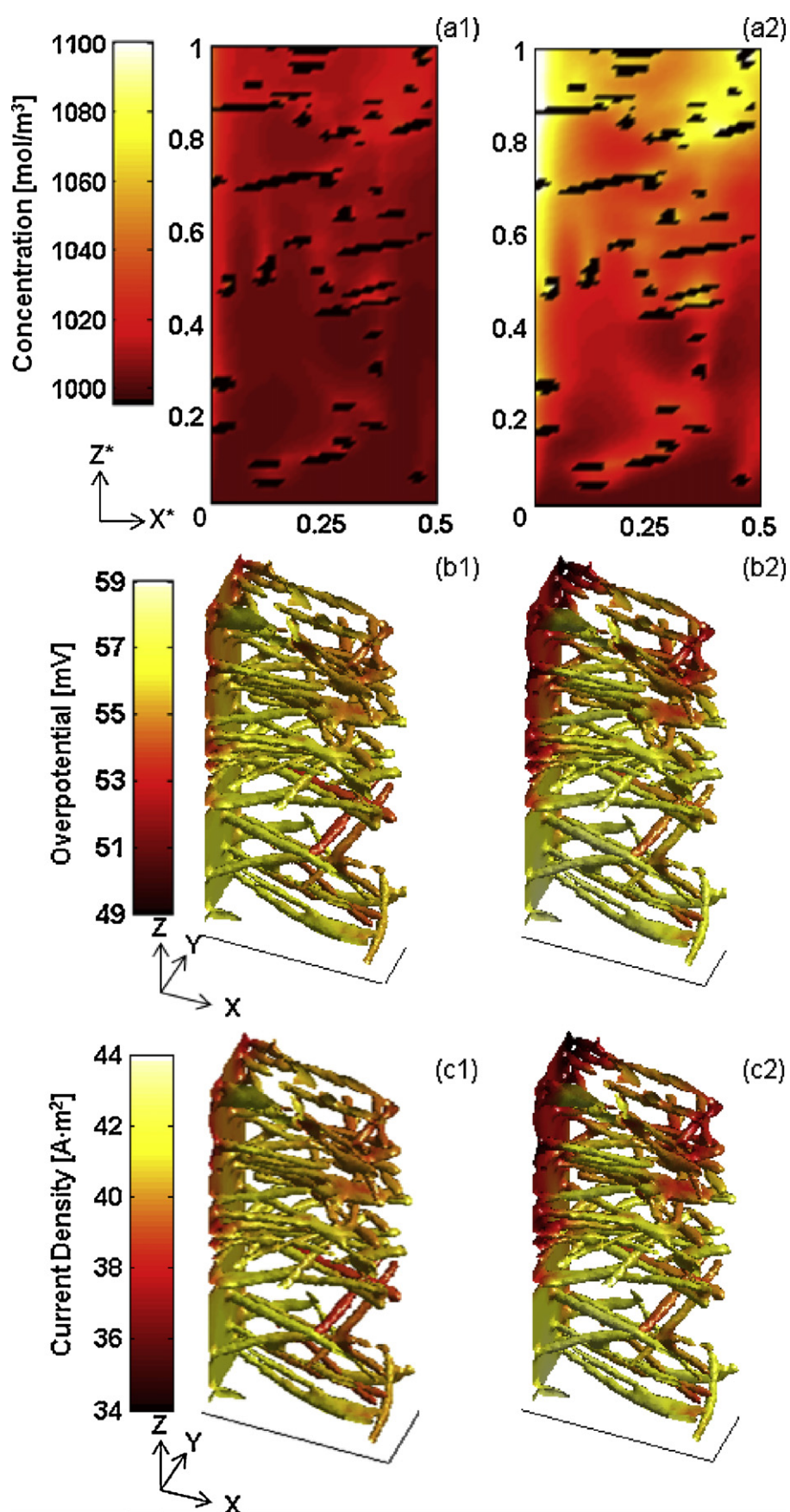
Fig. 15. Local distributions of (a) concentration, (b) overpotential, and (c) current density in the negative half cell corresponding to averaged electrolyte flow velocities of (1) 1.325 mm s^{-1} (baseline case) and (2) 0.264 mm s^{-1} with a specified inlet SOC of 50% during galvanostatic discharge at 400 A m^{-2}. Values are shown on the same range for comparison.
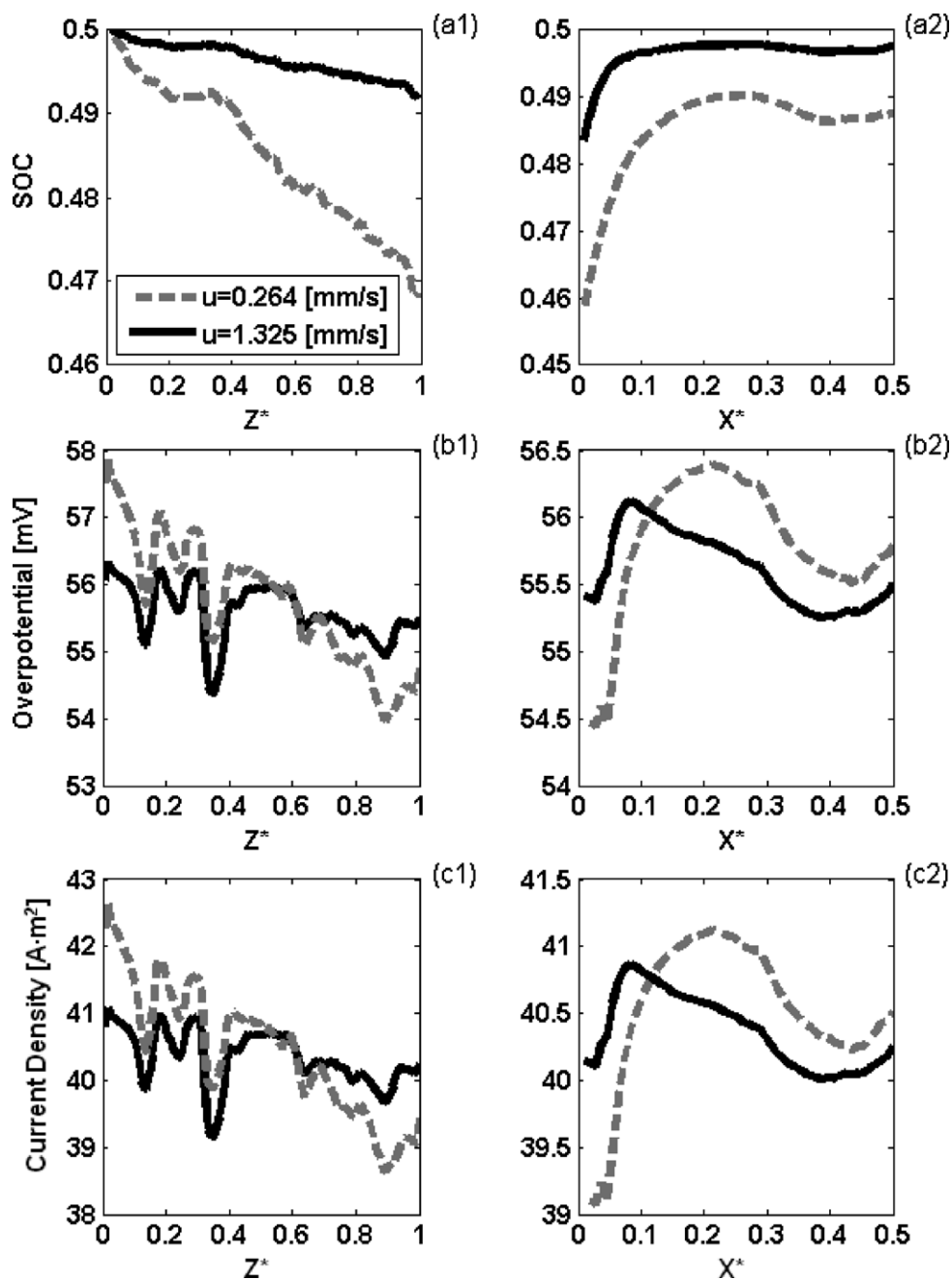
Fig. 16. Averaged distributions of (a) SOC, (b) overpotential, (c) current density about the (1) Z-direction and (2) X-direction in the negative half cell corresponding to averaged electrolyte flow velocities of 1.325 mm s^{-1} (black solid line) and 0.264 mm s^{-1} (dotted gray line) with a specified inlet SOC of 50% during galvanostatic discharge at 400 A m^{-2}.

reproducing the cell-level properties of volumetric models given the same operating conditions are observed. It should be noted that 140 mV is added to the cell voltage, a procedure adopted by You et al. [12]. This addition is to account for the potential difference across the membrane due to the difference in H$^+$ concentration between the positive and negative electrolytes as well as the contribution of the protons to the open circuit voltage at the positive electrode [30].

5.4. Detailed results for baseline XCT geometry

A survey of the results for the distribution of concentration, overpotential and current density will be presented for the baseline XCT geometry. Subject to the default parameters detailed in Tables 2–5, the operating cell voltage of the cell was 1.169 V.

A detailed examination into the species transport in the electrochemically active flow cell is visualized in Fig. 12a, where the local species concentrations of V^{3+} and VO^{2+} in the negative and positive half cells, respectively, are shown in the Y-midplane. It can be seen that the concentration near the inlet from the bottom of the domain remains unchanged from the specified Dirichlet value until it nears the proximity of a carbon fiber, where the electrolyte becomes electrochemically active (cross sections of the carbon fibers appear as dark features suspended in the cell). As a result, steep concentration gradients are observed near the active surface. As the electrolyte further proceeds along the height of the cell, gradual changes in bulk electrolyte concentration (as compared to the surface concentration in the electrolyte) can be detected as the reacting species diffuse/advect through the fluid. Note that due to the symmetry of the fiber structures, the distribution of local concentration is

similar in both half cells. The highest concentration change is found near the top of the current collectors.

The corresponding SOCs of the electrolytic species in both half cells along the Z- and X-directions are shown in Fig. 12b and c, respectively. Along the height in Fig. 12b, it can be seen that the concentration of both species in the electrolyte changes steadily from the specified value at the inlet. At the pore scale, this trend is subject to local fluctuations that depend on the density of active surfaces in a given Z-cross section. It is also apparent that this trend is generally linear, and so the consumption rate of electrolytic species is approximately constant along the height of the cell. In contrast, the averaged concentration profile along the length of the cell shown in Fig. 12c reveals that there is a steep concentration gradient close to the current collector. The high rate of electrochemical activity can be explained by a corresponding increase in the surface overpotentials that exist on the carbon fibers near the current collectors (as described in later sections). These trends in concentration are also observed from volumetric models in the literature [10,12].

Compared to volumetric models, however, the pore scale results offer much more detail about species transport in VRFB systems. The local effects of the carbon fibers in a flowing field of electrolyte shown in Fig. 12a are unable to be thoroughly studied in the continuum domains of volumetric models. Since bulk concentrations are solved for in volumetric models, the surface concentration of electrolyte must be approximated by empirical means (for use in the Butler–Volmer equation). However, since pore-scale models solve for the concentration field explicitly in the electrolytic phase, the value of surface concentration is directly available.

The overpotential at the surface of the electrode fibers serves as the primary impetus for electrochemical reactions in a VRFB. Using the pore-scale model, a 3-D distribution of the overpotential at the active surface of the electrode fibers is shown in Fig. 13a. For comparison, the magnitude of the overpotential is plotted (during discharge, the overpotential is negative in the positive half cell). This local distribution is dependent upon the operating parameters of the flow cell as well as the physical distribution of the fibers. It can be seen that the overpotential is higher on the fibers that are closer to the current collectors, and tends to decrease along the length of the fibers. It is interesting to note that near the top of the current collectors where the highest concentration changes are observed, overpotentials tend to be smaller. This indicates that one will expect to have higher overpotentials where there are more reactants available immediately near the surface of the electrode fibers.

Trends in the overpotential along the Z- and X-directions are shown in Fig. 13b and c, respectively. The Z-averaged plot reinforces the notion that overpotentials tend to decrease with decreasing SOC along the height of the half cell as shown in Fig. 12b for both negative and positive half cells. The X-averaged profile shows that overpotential tends to change more along the length of the half cell, and is generally higher closer to the current collectors except immediately adjacent to the current collectors, where there are large concentration gradients. The observed trends along the length and height of the half cell found in this pore-scale model are also echoed in the volume-averaged models, where the gradients in overpotential are primarily along the length of the cell [10,12].

The surface current density is obtained directly from the Butler–Volmer equation and provides information about the local fluxes of charge and species at the active surface of the electrode fibers. Fig. 14a shows the 3-D distribution of the local current density over the electrode surface for the entire cell. For comparison, the magnitude of the current density is shown on the same scale in the 3-D visualization (the current density in the positive half cell is always negative for discharge). It is apparent that the range in the current density in the positive half cell is larger compared to that of the negative half cell. This shows the sensitivity of the surface
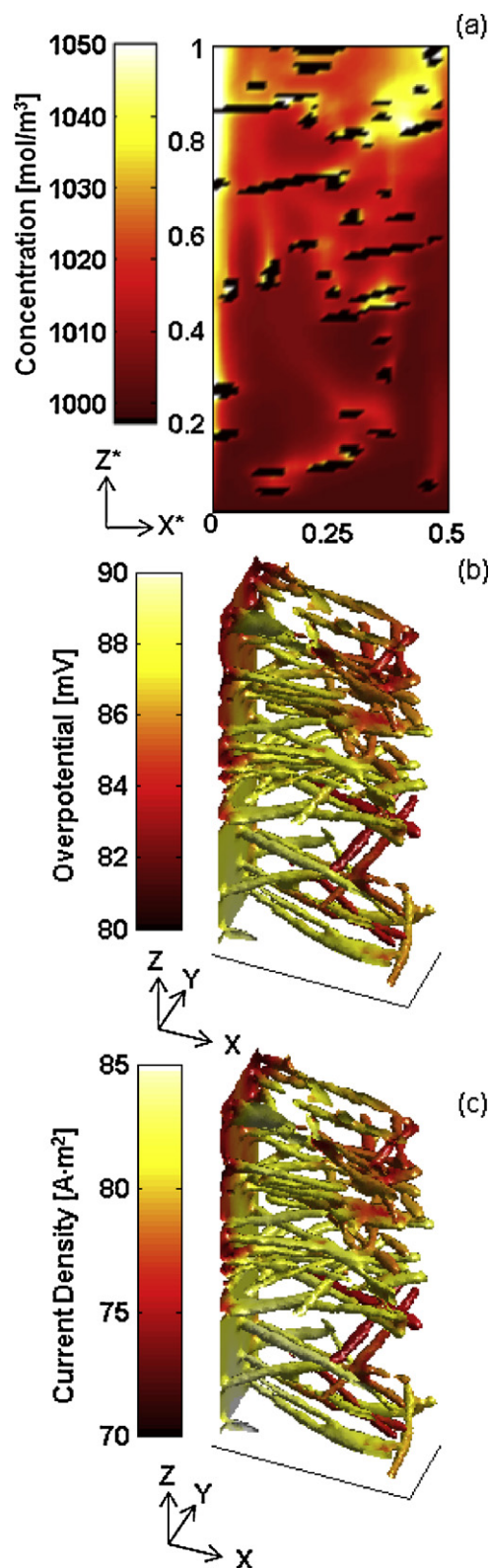

Fig. 17. Local distributions of (a) concentration, (b) overpotential, and (c) current density with a specified inlet SOC of 50% during galvanostatic discharge at 800 A m^{-2}.

current density to the operating parameters between the two sides, such as the Butler–Volmer rate constant. Similar to overpotential, the distribution of current density is subject to the local connectivity of the fibers. Also note that although the ranges in the current
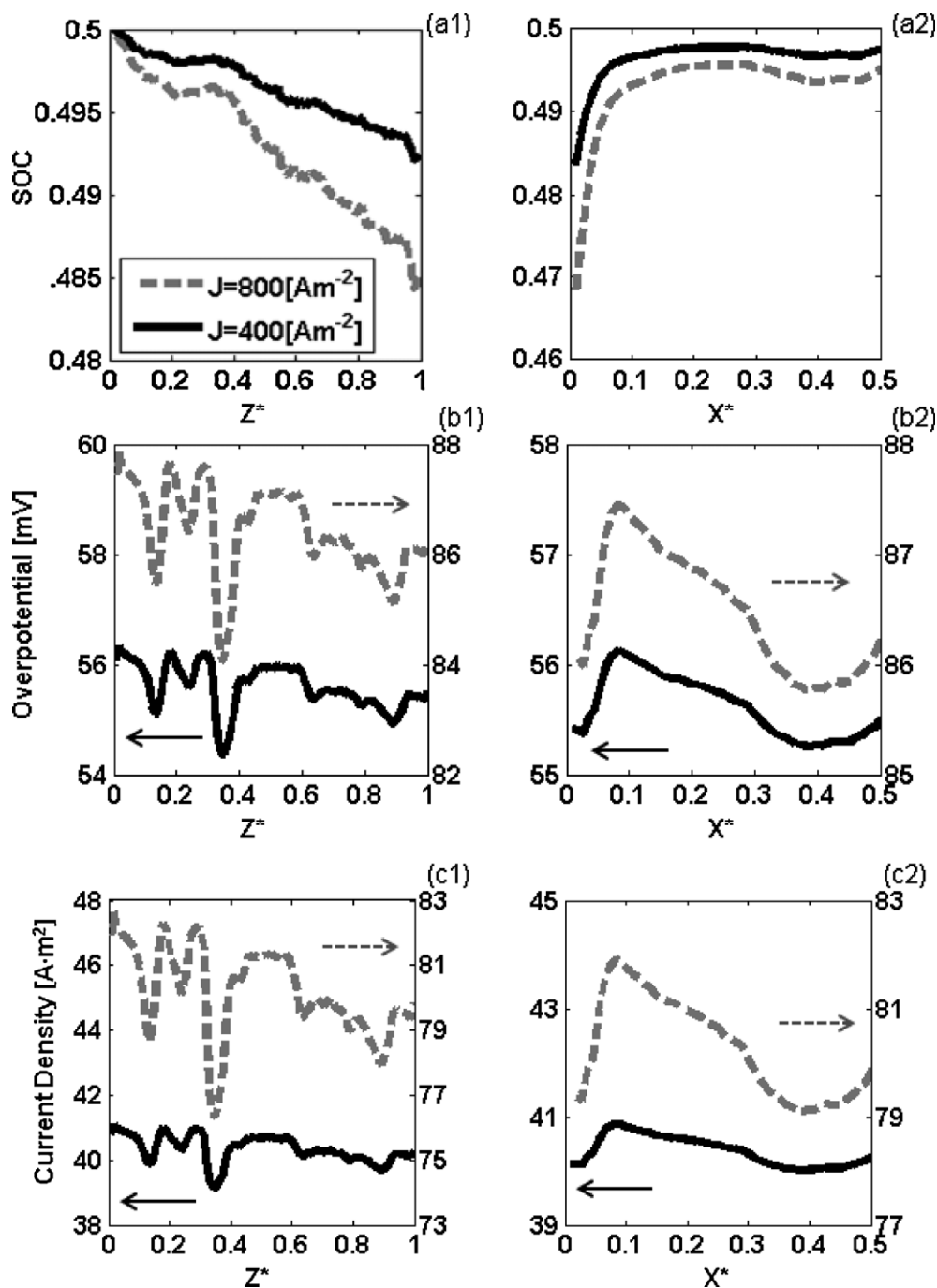
Fig. 18. Averaged distributions of (a) SOC, (b) overpotential, and (c) current density about the (1) Z-direction and (2) X-direction corresponding to an applied current density of 400 A m^{-2} (black solid line) and 800 A m^{-2} (dotted gray line) with a specified inlet SOC of 50%.

density on both sides are different, the mean current densities of the two sides are identical, as required by charge conservation.

Averaged distributions of the current density along the Z- and X-directions are shown in Fig. 14b and c, respectively. It is interesting to observe that these 1-D trends in current density are identical in shape to the trends observed for overpotential, indicating that sites of high overpotential will also be sites of high current density, and consequently regions of high electrochemical activity. In volumetric models, the distribution of current density primarily varies along the length of the cell, and remains unchanged in the height [10,12]. Here, however, notable trends are observed in both directions within the half cells.

5.5. Effect of flow rate on cell performance for XCT geometry

The flow rate is a critical operating parameter in VRFB systems. If the flow is too slow, the transport of species in the electrolyte will not be as effective, while a flow that is too fast may induce large parasitic pumping losses. In this section, the effects of fluid velocity on both local and averaged species concentration, overpotential, and current density are investigated, and the results are compared to those of the baseline case presented in the above section. An average inlet velocity of 0.264 mm s^{-1} (a five-fold decrease compared to the baseline case), corresponding to a Reynold's number of 0.0362, is used in the test case.

The local distributions of concentration, overpotential and current densities in the negative half cell are shown in Fig. 15 while the averaged profiles are shown in Fig. 16. It can be seen from the concentration distributions in Fig. 15a that there are significantly larger concentration gradients in the slower flow rate case. However, the larger concentration gradients are purely a consequence of the inhibited advection of fresh electrolyte in the case of the slower fluid velocity; the total amount of species consumed must be the same in both cases (since the external current applied is the same). The factor by which concentration changes between two cases is roughly the same as the factor by which the velocity changed. It can be seen from Fig. 16a1 that on average, the concentration change in the Z-direction is 4 times larger for the slower flow case, which is close to the factor of 5 by which the velocity decreased. It is also evident that the SOC at any point in the height of the baseline case is roughly the same as the SOC at 1/4 of that height for the low flow rate case. This implies that the species transport in the electrolyte is a largely convection-dominant process. If the flow is unidirectional and the species transport is purely convection-driven, then the change in concentration will change by the exact factor as the change in velocity.

Shown on the same scales in Fig. 15b and c, it is evident that the 3-D distributions of overpotential and current density are amplified slightly in the slower flow rate case. Larger gradients of both quantities can be seen near the current collector and in localized clusters of fibers. From Fig. 16c, it can be seen that the averaged current density does indeed fluctuate about the same mean value in both cases, as previously mentioned. A similar observation can be made for the overpotential as seen in Fig. 16c. In the vertical direction, larger overpotentials and current densities are found close to the inlet of the cell for slower flow rates, signifying that more reactions are occurring in that region.

The cell voltage for the new case was 1.166 V, showing that decreasing the flow rate in this case degraded the cell performance. A greater uniformity in the species distribution ensures a higher SOC of the electrolyte at the active surface, and lower overpotentials and current densities are required to drive the electrochemical reaction. A case with a lower flow rate disrupts this uniformity, and higher overpotentials are needed to discharge the cell at the same rate, effectively reducing the cell performance.

5.6. Effect of external current on cell performance for XCT geometry

The effect of the applied discharge current density on the flow cell relative to the baseline case is investigated in this section using an increased current density of $800 \, \text{A m}^{-2}$. The local distributions of concentration, overpotential and current density for the negative half cell are shown in Fig. 17, and can be compared to the results from the baseline in Section 5.4. The averaged profiles of these values are shown in Fig. 18. From the concentration distributions shown in Fig. 16a, it is evident that with a larger drawing current, one will expect to have larger consumption rates of fuel in the electrolyte. In fact, under the same operating conditions, the consumption rate must be proportional to the rate of the drawing current in order to satisfy charge conservation. This is seen most clearly in Fig. 18a1, where the SOC along the height of the cell in the baseline case is approximately half that of the case with the higher drawing current.

A decreased cell voltage of 1.116 V is attained from the higher current density case, indicating a degradation in cell performance. From the local and average distributions, it is evident that the magnitude as well as the gradient of the overpotential and current density increased in the case of the larger drawing current. As expected from charge conservation, the magnitude of the current

density is doubled for the test case compared to the baseline; a similar trend is observed in the volumetric model of You et al. [12].

6. Conclusions

A 3-D pore-scale model has been developed to simultaneously solve for the coupled fluid, species, and charge transport as well as electrochemistry in vanadium redox flow batteries (VRFB) based on XCT-reconstructed geometry of real carbon-felt electrode materials. Unlike existing volume-averaged models, which simulate the electrochemical processes within a continuum domain, pore-scale modeling distinguishes between the solid electrode and liquid electrolyte phase in the flow cell, thus capturing the effects of electrode geometry on cell performance.

The cell voltage and overpotential for idealized geometries as a function of the active surface area and the state of charge (SOC) are examined first and the results are compared with a simplified model based on charge conservation, as well as those obtained using volume-averaged models. The pore-scale model is then used to study the averaged and local species concentration, overpotential, and current density based on detailed XCT geometries. The performance predictions from the present model show good agreement with macroscopic models and experimental observations. However, the pore-scale model provides valuable information inside the porous electrode for loss detection and will aid in optimizing electrode microstructures and flow designs for VRFBs. Future work will focus on examining the effects of assembly-induced compression and flow configurations on the performance of VRFBs.

Appendix A. Nomenclature

A	surface area of electrode fibers [mm^2]
A^*	ratio of active surface area to current collector area
C	concentration [mol m^{-3}]
D	diffusivity [m^2 s^{-1}]
$\boldsymbol{e}$	discrete velocities in the D3Q19 model
E	effective voltage [V]
E^0	open circuit voltage [V]
f	particle velocity distribution function
F	Faraday's constant [C mol^{-1}]
H	total cell height [mm]
$\mathbf{J}$	current density [A m^{-2}]
l	half cell length [mm]
L	average pore size [μm], total cell length [mm]
$\hat{\mathbf{n}}$	surface unit normal
$\mathbf{N}$	mole flux [mol m^{-2}]
p	fluid pressure [Pa]

R	universal gas constant [$J\,mol^{-1}\,K^{-1}$]
Re	Reynold's number
SOC	state of charge
T	operating temperature [K]
u	velocity of the electrolyte flow [$m\,s^{-1}$]
u′	averaged LBM fluid velocity
V	half cell volume [mm^3]
w	weight factors
W	total cell width [mm]
x	discrete lattice coordinate
X	component in the X direction [mm]
Y	component in the Y direction [mm]
z	valence
Z	component in the Z direction [mm]

Greek letters

α	transfer coefficient
η	overpotential [V]
ϕ	potential [V]
κ	conductivity [$S\,m^{-1}$]
ν	electrolyte kinematic viscosity [$m^2\,s^{-1}$]
ρ	electrolyte density [$kg\,m^{-3}$]
τ	relaxation time

Subscripts

1	reaction (1)
2	reaction (2)
α	discrete lattice direction
a	anodic reaction quantity
avg	average quantity
c	cathodic reaction quantity
eff	effective property
ext	externally applied quantity, current collector quantity
f	fixed charge site quantity
j	species $j \in \{V(II), V(III), V(IV), V(V), H^+, H_2O, SO_4^{2-}\}$
mem	ion-exchange membrane quantity
s	solid fiber phase property

Superscripts

*	dimensionless quantity
0	total or initial quantity

eq	equilibrium state
in	cell inlet value
s	surface property
+	positive half cell quantity
–	negative half cell quantity

References

[1] M. Skyllas-Kazacos, M. Rychcik, R. Robin, A.G. Fane, J. Electrochem. Soc. 133 (1986) 1057.
[2] E. Sum, M. Rychcik, M. Skyllas-Kazacos, J. Power Sources 16 (1985) 85.
[3] E. Sum, M. Skyllas-Kazacos, J. Power Sources 15 (1985) 179.
[4] M. Pourbaix, Atlas of Electrochemical Equilibria in Aqueous Solutions, 2nd ed., NACE International, Houston, 1974.
[5] D.R. Lide, CRC Handbook of Chemistry and Physics, 83rd ed., CRC Press, Boca Raton, FL, 2002.
[6] J. Larminie, A. Dicks, Fuel Cell Systems Explained, 2nd ed., John Wiley and Sons, 2002.
[7] H. Al-Fetlawi, A.A. Shah, F.C. Walsh, Electrochim. Acta 55 (2009) 78.
[8] H. Al-Fetlawi, A.A. Shah, F.C. Walsh, Electrochim. Acta 55 (2010) 3192.
[9] A.A. Shah, H. Al-Fetlawi, F.C. Walsh, Electrochim. Acta 55 (2009) 1125.
[10] A.A. Shah, M.J. Watt-Smith, F.C. Walsh, Electrochim. Acta 53 (2008) 8087.
[11] M. Vynnycky, Energy 36 (2010) 2242.
[12] D. You, H. Zhang, J. Chen, Electrochim. Acta 54 (2009) 6827.
[13] K.N. Grew, A.S. Joshi, A.A. Peracchio, W.K.S. Chiu, J. Power Sources 195 (2010) 2331.
[14] J.R. Izzo Jr., A.S. Joshi, K.N. Grew, W.K.S. Chiu, A. Tkachuk, S.H. Wang, W. Yun, J. Electrochem. Soc. 155 (2008) B504.
[15] A.S. Joshi, K.N. Grew, J.J.R. Izzo, A.A. Peracchio, W.K.S. Chiu, J. Fuel Cell Sci. Technol. 7 (2010) 011006.
[16] A.S. Joshi, K.N. Grew, A.A. Peracchio, W.K.S. Chiu, J. Power Sources 164 (2007) 631.
[17] N. Shikazono, D. Kanno, K. Matsuzaki, H. Teshima, S. Sumino, N. Kasagi, J. Electrochem. Soc. 157 (2010) B665.
[18] P.P. Mukherjee, C.Y. Wang, Q. Kang, Electrochim. Acta 54 (2009) 6861.
[19] J. Park, X. Li, J. Power Sources 178 (2008) 248.
[20] P. Rama, Y. Liu, R. Chen, H. Ostadi, K. Jiang, J. Fuel Cell Sci. Technol. 7 (2010) 031015.
[21] R. Ferrigno, A.D. Stroock, T.D. Clark, M. Mayer, G.M. Whitesides, J. Am. Chem. Soc. 124 (2002) 12930.
[22] D.M. Bernardi, M.W. Verbrugge, AIChE J. 37 (1991) 1151.
[23] T.N.W. Yamamura, T. Yano, Y. Shiokawa, J. Electrochem. Soc. 152 (2005) A830.
[24] X. He, Q. Zou, L.S. Luo, M. Dembo, J. Stat. Phys. 87 (1997) 115.
[25] T. Inamuro, M. Yoshina, F. Ogino, Phys. Fluids 7 (1995) 2928.
[26] Q. Zou, X. He, Phys. Fluids 9 (1997) 1591.
[27] Q. Zou, S. Hou, G.D. Doolen, J. Stat. Phys. 81 (1995) 319.
[28] Z. Guo, C. Zheng, B. Shi, Phys. Fluids 14 (2002) 2007.
[29] S.V. Patankar, Numerical Heat Transfer and Fluid Flow, McGraw-Hill, 1980.
[30] K.W. Knehr, E.C. Kumbur, Electrochem. Commun. 13 (2011) 342.